

Evolution of granular materials under isochoric cyclic simple shearing

Ming Yang* and Mahdi Taiebat†

Department of Civil Engineering, University of British Columbia, Vancouver BC V6T1L7, Canada

Patrick Mutabaruka‡ and Farhang Radjai§

CNRS, University of Montpellier, LMGC, 34090 Montpellier, France (Received 18 September 2020; revised 4 February 2021; accepted 10 March 2021; published 18 March 2021)

By means of 3D particle dynamics simulations, we analyze the microstructure of granular materials subjected to isochoric (constant volume) cyclic shearing, which drives the system towards a liquefaction state characterized by loops of jamming-unjamming transition with periodic loss of strength and irreversible accumulation of shear strain. We first show that the macroscopic response obtained by these simulations agrees well with the most salient features of the well-known cyclic behavior of granular materials both before and after liquefaction. Then we investigate the evolution of particle connectivity, force transmission, and anisotropies of contact and force networks. The onset of liquefaction is marked by partial collapse of the force-bearing network with rapid drop of the coordination number and nonrattler fraction of particles, and significant broadening of the contact force probability density function, which begins in the preliquefaction period. We find that the jamming transition in each cycle occurs for a critical value of the coordination number that can be interpreted as the percolation threshold of the contact network and appears to be independent of the initial mean stress, void ratio, and cyclic shear amplitude. We show that upon unjamming in each cycle an isotropic loss of contacts occurs and is followed by the development of high contact anisotropy and a large proportion of particles with only two or three contacts. The higher mobility of the particles also involves a lower degree of frustration of particle rotations and thus lower friction mobilization and tangential force anisotropy. These findings are relevant to both undrained cyclic deformations of saturated soils and rheology of dense non-Brownian suspensions where volume change is coupled with pore liquid drainage conditions.

DOI: [10.1103/PhysRevE.103.032904](https://doi.org/10.1103/PhysRevE.103.032904)**I. INTRODUCTION**

Granular materials are known to exhibit both solid-like and fluid-like behaviors depending on the history of deformations and stresses to which they are exposed, their interactions with a pore-filling fluid, and loading conditions [1,2]. In soil mechanics, the transition from solid-like to fluid-like state is of paramount importance as it may lead to catastrophic loss of soil strength, large irreversible strains, and significant damage to civil engineering structures. For example, sudden disturbance of loose granular soil by an earthquake leads to its compaction. The compaction is, however, inhibited if the soil is saturated by water that due to a low soil permeability can not be quickly drained, leading thereby to load transfer from interparticle force chains to the pore water. This phenomenon, known as “soil liquefaction,” is the origin of many landslides in coastal and mountainous areas [3–5]. Such undrained conditions occur in granular soils with low permeability (silty sands or gravels containing finer sediments) when subjected to shaking or cyclic deformations. Quicksands behave in a similar fashion.

The rheology of soils under cyclic loading both before and after liquefaction has been extensively explored and modeled in recent decades (e.g., Refs. [6–9]). The issue is whether the soil keeps the memory of the conditions (such as initial pressure p_0 , shear stress cycle amplitude, solid fraction, etc.) that led to its first liquefaction and how much it can deform when subjected to a new loading path. Motivated by macroscopic observations from laboratory experiments, continuum-based elastoplasticity models have also been developed and applied to liquefaction-related applications (e.g., Refs. [10–13]). Nevertheless, the physical particle-scale mechanisms governing the long-time evolution of the microstructure that underlies transition to the liquefaction state and its further mobility after the initial liquefaction remains to a large extent unexplored.

The transition of granular materials from a stable solid-like state to a flow state has been at the focus of many studies in physics, often described as a jamming-unjamming transition [14–17]. Most of the time, however, this term refers to a transition arising from monotonic increase or decrease of shear stress or shear strain. The case of soil liquefaction provides a more complex example of such a transition occurring in response to cyclic loading. Note, however, that, although soil liquefaction arises from load transfer between soil and water, this phenomenon does not need a saturated granular material or dynamic conditions, but can occur in a dry granular material under isochoric (constant volume) and quasistatic

*yangm15@civil.ubc.ca

†mtaiebat@civil.ubc.ca

‡patrick.mutabaruka@umontpellier.fr

§franck.radjai@umontpellier.fr

loading conditions. For this reason, isochoric cyclic shearing has often been used as a proxy for the undrained cyclic deformation of liquid-saturated granular materials subjected to isobaric (constant total stress) conditions [18–20]. At constant volume, when the solid fraction Φ is not too low, a monotonic increase of the shear stress τ will entail a gradual increase of the mean stress p proportionally to τ after a small shear deformation because of hindered dilatancy. By contrast, if monotonic shearing is replaced by cyclic shearing of small shear stress or shear strain amplitude for the same solid fraction, p will gradually decrease, and after several cycles will suddenly drop to a much lower value by loss of stability and unjamming of the particles. Under continued shear cycling, the jamming-unjamming process will be repeated in each cycle with irreversible shear strain accumulation.

An in-depth investigation of the long-time evolution of granular microstructure under cyclic shearing is currently only possible by discrete element method (DEM) simulations based on the integration of the equations of motion for all particles by accounting for frictional contact interactions between particles [21]. The application of DEM to carry out isochoric tests leading to liquefaction dates back to Ref. [22], who successfully verified the possibility of reproducing cyclic liquefaction by simulations. Later simulations have also convincingly shown that DEM simulations in three dimensions capture well all the macroscopic features of cyclic shearing and transition to cyclic liquefaction at constant volume [23–25]. An important parameter of cyclic shearing is the potential for liquefaction or “liquefaction resistance” [26], which is measured by the number of cycles N_{IL} required to reach the first liquefaction cycle (initial liquefaction). Both experiments and simulations show that N_{IL} declines (lower liquefaction resistance) for higher amplitude of cyclic strain due to the larger rearrangements of the granular fabric, and hence stronger loss of contacts, in each cycle [23,27,28]. A similar trend is observed when cyclic shear stress is imposed instead of cyclic shear strain, although the rearrangements prior to liquefaction may be small in this case [19].

Simulations have also been used to show that the liquefaction transition is a consequence of mechanical instability at the so-called “phase transformation” state where the behavior switches from contraction to dilation during isochoric monotonic shearing [25]. Hindered dilation (due to constant volume) leads to jamming and rebuilding of the contact network, whereas hindered contraction leads to an unstable stress state and unjamming of the particles. The coordination number appears thus as a natural descriptor of this transition. It has been suggested that instability occurs when the coordination number drops below its isostatic value [20,25]. But all the reported simulations show that the coordination number never vanishes. This observation contradicts, however, the full vanishing of the mean stress often assumed for liquefaction since the mean stress is proportional to the mean force, and therefore zero mean force would imply also the vanishing of the coordination number!

Several authors have also investigated the contact network anisotropy and force anisotropy during cyclic shearing [24,25,27]. The contact network anisotropy (or fabric anisotropy) may increase dramatically in liquefaction state, reflecting the lower values of the coordination number and

unstable particle arrangements. The simulations show that the normal force anisotropy prevails in the liquefaction state as compared to the fabric anisotropy and tangential force anisotropy. However, these features have never been analyzed during shear cycles before and after liquefaction and discussed in connection with the coordination number. In fact, a full analysis of the fabric evolution during cyclic shearing requires its representation in the space of coordination number vs. fabric anisotropy [29]. Besides fabric and force anisotropies, it has also been suggested that, given the sparse nature of the contact network in the liquefaction state, the fabric parameters should account for the neighborhood of the particles rather than their contacts [30,31].

In this paper, we analyze both the long time and short time (within a cycle) evolution of the contact and force networks by means of extensive long-time DEM simulations of 3D packings composed of spherical particles under isochoric cyclic simple shearing. For the long time behavior, we would like to better understand how the particles’ connectivity evolves with shear stress, mean stress, and shear strain. Besides the coordination number, we study the connectivity diagram defined as the proportions P_c of particles with exactly c contacts, and the proportion of nonrattler particles, i.e., particles that belong to the force-bearing network. We are also interested in the jamming-unjamming transition within each shear cycle before and after liquefaction transition, and how the fragile system rebuilds into a stable network. As we shall see, the coordination number is a key parameter for this transition, although not in terms of mechanical stability but as a percolation threshold prompting transition to the jammed state and sustaining the shear stress. We also consider the contact force PDFs, which have not been analyzed in the past, to evidence the signature of cyclic shearing and transition to the liquefaction state. As we shall see, the force distributions are increasingly more inhomogeneous while keeping their common exponential shape for forces above the mean force. The statistical distributions of local variables such as friction mobilization at characteristic states will provide new insights into the process of transition to the liquefaction state. Finally, we analyze the role of the fabric and force anisotropies in relation to the particle connectivity and development of shear stress during jamming transition in each cycle.

In the following, in Sec. II the DEM contact model, sample preparation and simulation procedures are described. In Sec. III the macroscopic response is presented in terms of stress path and stress-strain loop for a representative simulation. The evolution of granular microstructure in this simulation is explored in terms of particle connectivity, force transmission, and fabric and force anisotropies in Sec. IV. In Sec. V the effects of the initial and loading conditions on the evolution of particle connectivity and anisotropies are investigated. Finally, we summarize the findings and sketch potential perspectives for this work.

II. NUMERICAL PROCEDURE

A. Contact model

An in-house 3D particle dynamics DEM numerical platform, named GRFlow3D [32], was used in this work. The

granular assembly was simulated using spheres interacting via soft contact laws. The contact interactions between spheres consist of normal collision, tangential sliding, rolling and torsion, and the key quantity is the elastic deflection between particles, $\delta_{[]}$, from which the corresponding force $\hat{f}_{[]}$ can be calculated using a linear spring-dashpot model:

$$\hat{f}_{[]} = -k_{[]}\delta_{[]} - c_{[]}\dot{\delta}_{[]}, \quad (1)$$

where $k_{[]}$ is the spring stiffness, and $c_{[]}$ is the viscous dashpot coefficient. The subscript placeholders can be for n (normal contact), t (tangential sliding), r (rolling), or o (torsion). Given the radii of two particles, a_i , a_j and their positions, \mathbf{r}_i , \mathbf{r}_j , the normal contact deflection δ_n along the normal direction is the overlap between the two particles, given by

$$\delta_n = \|\mathbf{r}_i - \mathbf{r}_j\| - a_i - a_j. \quad (2)$$

The interparticle forces and torques exist only when $\delta_n < 0$. To exclude the nonrealistic attractive force due to viscous damping at incipient separation between two particles, the normal force f_n is represented by a ramp function $R(\hat{f}_n)$ where $R(x) = x$ if $x > 0$ and $R(x) = 0$ if $x \leq 0$. The tangential force f_t is equal to \hat{f}_t if $|\hat{f}_t| < \mu_t f_n$ and as $\text{sgn}(\hat{f}_t)\mu_t f_n$ if $|\hat{f}_t| > \mu_t f_n$. Calculating the rolling and torsional forces (torques) is analogous to the tangential force. Unlike the normal deflection δ_n , the other three elastic deflections cannot be directly calculated, but should be cumulated by integration over time from the moment two particles come to contact, as explained in detail in Refs. [21,33].

Once all the forces and torques on a particle are obtained, the translational and rotational accelerations can be calculated using Newton's second law of motion. These accelerations, together with the particle velocities at the beginning of each time step are then used to update the velocities and positions of all particles. We used a velocity-Verlet time-stepping scheme in our simulations.

B. Sample preparation and shearing protocols

The simulations of isochoric simple shearing involve two steps: (1) preparing particle assemblies via isotropic compression condition and (2) applying cyclic simple shear mode to these assemblies under isochoric condition. The constructed samples consist of spheres with low polydispersity, i.e., $d_{\max}/d_{\min} = 2$ where $d_{\min} = 1.0$ mm and d_{\max} refer to the minimum and maximum particle diameters, respectively. Between d_{\min} and d_{\max} , the particle size follows a uniform distribution of particle volumes, so that the number of particles belonging to a class of diameter d is proportional to d^{-3} . One can refer to Refs. [34,35] for details of generating the particle size distribution. Once the particles are generated, they are placed randomly on a 3D sparse lattice to avoid the overlap. This 3D lattice is contained in a rectangular cell whose top and bottom sides are rigid walls, and the four lateral sides are periodic boundaries. This setting is denoted as a biperiodic simulation cell.

The samples are compressed isotropically by moving the six sides of the cell. During the compression process, the gravity is set to zero to avoid stress gradients. The six sides of the cell follow a translational move. The tangential friction coefficient μ_t is tuned to achieve a given value of void ratio

e , defined as the ratio of the total pore volume to the solid volume. One has $e = 1/\Phi + 1$, where Φ is the solid fraction. Many of the laboratory procedures for sample preparation at different densities can not be precisely simulated; therefore, we adopted a simple computational procedure, modified from Refs. [19,36], to prepare samples comparable with the laboratory ones. The procedure consists of four substeps, which we describe here by taking the case of constructing a medium dense sample with the target mean stress $p_0 = 100$ kPa: (1) with $\mu_t = 0.20$, densifying the sparse sample by moving the six sides at a constant velocity until the void ratio e reaches 1.0; (2) setting velocities of particles and the six sides to zero, and using a servo-control algorithm to compress the sample isotropically with the target $p = 10$ kPa where μ_t remains 0.2; (3) increasing the target p to half of p_0 , i.e., 50 kPa, and continuing compression of the sample with $\mu_t = 0.20$; (4) modifying μ_t to 0.5 used for further compressing the sample with the target $p = p_0 = 100$ kPa and subsequent cyclic shearing. Readers can refer to Refs. [37,38] for the detail of servo-control algorithm. The first three substeps generate an initially dense packing by controlling the tangential friction coefficient and increasing the confinement. The last step is necessary to obtain a smooth distribution of $f_t/(\mu_t f_n)$ between 0 and 1, as usually a different value of μ_t is used in the step of cyclic shearing. We conducted other simulations on samples with different numbers of spheres ranging between 2197 and 10648. We did not see much difference in the macroscopic response under isochoric cyclic shearing. Hence, samples with 8000 spheres were used in this study, falling into a range similar to those presented in Refs. [19,20]. Figure 1(a) displays one of the samples prepared by the above procedure.

In the step of isochoric cyclic simple shearing, the sample volume is maintained constant by fixing four lateral sides and the bottom wall and keeping the sample height constant. Cyclic simple shearing is undertaken by moving the top wall horizontally at a constant velocity v_x . To reduce possible slippage between the walls and the sample, one layer of particles is glued to the top and bottom walls, respectively, as indicated by gray spheres in Fig. 1(b). The shear direction is reversed each time the shear stress τ extracted from the calculated stress tensor, as explained below, reaches a target amplitude τ^{amp} . This corresponds to the so called "uniform amplitude cyclic simple shear test" [19]. In soil mechanics, a dimensionless quantity named "cyclic stress ratio" (CSR) is used to quantify the cyclic shearing intensity, defined by the ratio

$$\text{CSR} = \frac{\tau^{\text{amp}}}{p_0}, \quad (3)$$

where p_0 is the initial mean stress. Table I summarizes the simulated isochoric cyclic simple shear tests. T1, T2, and T3 are configured by varying the initial void ratio e of samples, T2, T4, and T5 are different in the initial mean stress p_0 , while T2, T6, and T7 are conducted for different values of CSR. In this study, we consider simulations of samples with a void ratio between 0.629 and 0.670. Very dense systems get jammed under shearing at constant volume, and very loose samples can easily become fluid-like even without the shear stress reaching the targeted value of CSR. To expand the ranges of void ratio in cyclic shearing, lower values of CSR should be used.

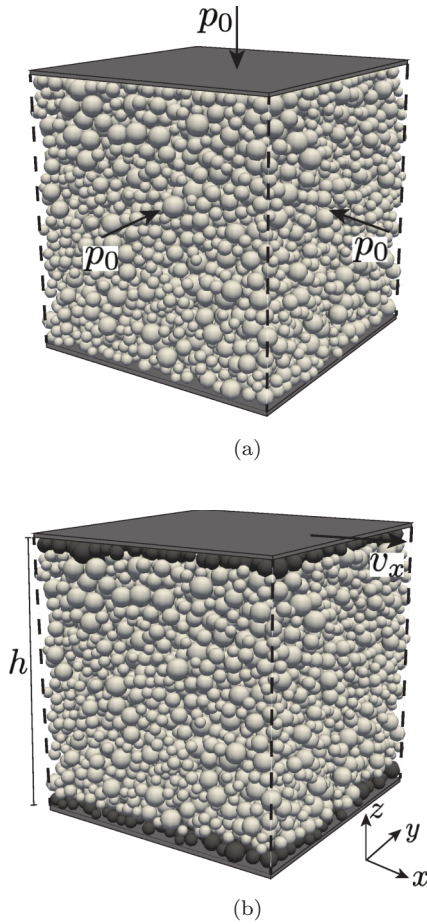


FIG. 1. Illustration of particle arrangements and boundary conditions for a sample composed of 8000 particles: (a) at the end of sample preparation; (b) during constant height cyclic shearing. The gray particles are glued to the top and bottom walls of the simulation cell.

To choose the shear rate, we consider the inertial number $I = \dot{\gamma}d\sqrt{\rho/p}$, where $\dot{\gamma} = |v_x|/h$ is the shear strain rate with h the sample height, ρ the density of particles, and d the mean particle diameter. The shear is nearly quasistatic if $I \ll 1$ [39], and typically the threshold is chosen as 10^{-3} . In isochoric cyclic shearing, I varies due to the change of p . After liquefaction transition, p degrades cyclically to vanishingly small values due to unjamming, and hence I may increase beyond 10^{-3} whatever its value before unjamming. For a range of velocities v_x of the top wall between 0.005 m/s and

TABLE I. Simulated cyclic simple shear tests.

ID	$e(-)$	p_0 (kPa)	CSR (-)
T1	0.629	100	0.25
T2	0.647	100	0.25
T3	0.670	100	0.25
T4	0.647	200	0.25
T5	0.647	600	0.25
T6	0.647	100	0.20
T7	0.647	100	0.30

TABLE II. DEM parameters.

Description	Value
Density, ρ	2650 kg/m ³
Normal stiffness, k_n	10 ⁶ N/m
Normal viscosity, c_n	1.15 kg/s
Tangential stiffness, k_t	0.8 k_n
Tangential viscosity, c_t	0.2 c_n
Tangential friction coefficient, μ_t	0.5 ^a
Rolling stiffness, k_r	0.1 k_n
Rolling viscosity, c_r	0.05 c_n
Rolling friction coefficient, μ_r	0.1
Torsion stiffness, k_o	0.1 k_n
Torsion viscosity, c_o	0.05 c_n
Torsion friction coefficient, μ_o	0.1

^aCyclic shearing step.

0.01 m/s, we found that the macroscopic response even in the liquefaction state does not change noticeably during the whole shearing process, and I remains below 10^{-3} for jammed states and below 0.025 for unjammed states. Therefore, in all the simulations reported in this paper, we set $v_x = 0.01$ m/s, corresponding to a shear rate $\dot{\gamma} \approx 0.38$ s⁻¹ and consistent with Ref. [20]. For this choice, the simulations are faster, and at the same time shearing is quasistatic during jammed states. The higher values of I at unjamming arise from unstable deformation, which in our simulations is an intrinsic feature of cyclic liquefaction only and not influenced by the loading rate.

The simulation parameters are given in Table II. One can introduce the stiffness number κ such that the average normal deflection δ_n satisfies $\delta_n/d \propto \kappa^{-1}$ [21]. For the linear contact law in the normal direction, $\kappa = k_n/(pd)$. In this study k_n is chosen as 10^6 N/m to guarantee $\delta_n \sim 10^{-3}d$ in each contact, i.e., the particles can be considered as nearly undeformable [35]. Then c_n is determined to attain a value of 0.15 for the normal coefficient of restitution based on Ref. [40]. $\mu_t = 0.5$ is a common value of the friction coefficient [25,41,42]. The values for other microscopic material parameters can be obtained from their relations to k_n , c_n or μ_t suggested by Luding [33] and listed in Table II. The rolling and torsion stiffnesses and their friction coefficients were set to a small nonzero value (0.1) as a simple way to enhance dissipation while sliding friction with its higher coefficient (0.5) remains the main effect. Rolling friction has a stabilizing effect on the simulations, it allows for higher normal force anisotropy and more pronounced force chains, features that are generally induced by aspherical particle shape [21].

III. MACROSCOPIC RESPONSE

At the sample scale, stresses and strains in the cyclic shearing phase are analyzed to monitor mean stress degradation and shear strain development. The stress tensor σ of the granular assembly can be expressed as a function of the microscopic interactions between particles over a selected volume V :

$$\sigma = \frac{1}{V} \sum_{c \in N_c} l^c \otimes f^c, \quad (4)$$

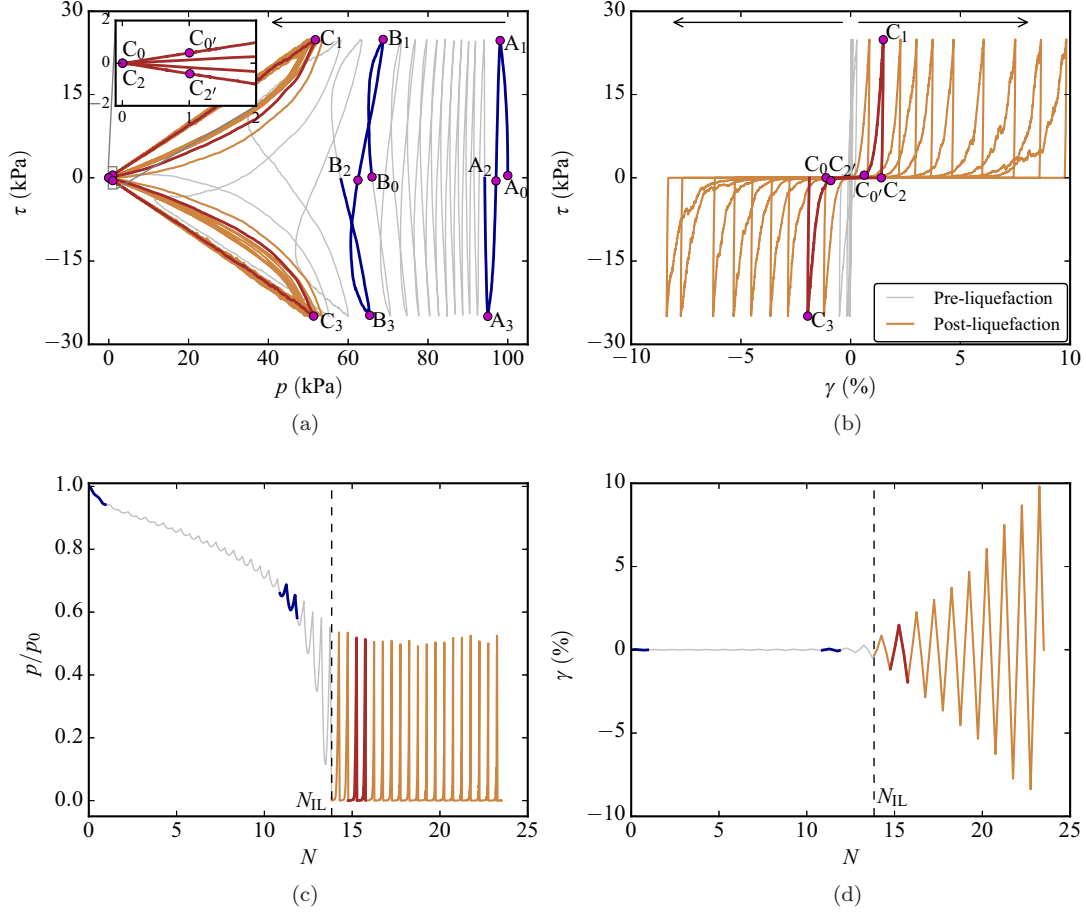


FIG. 2. Macroscopic response of isochoric cyclic simple shear test T2 in Table I: (a) stress path; (b) stress-strain curve; (c) normalized mean stress evolution; (d) shear strain development.

where \mathbf{l}^c is the branch vector connecting the centers of two particles for interior contact or connecting the particle center and the contact point for exterior contacts, \mathbf{f}^c is the contact force, \otimes denotes the dyadic tensor product, and the summation runs over all the contacts N_c in the selected volume V . The superscript c in \mathbf{l}^c and \mathbf{f}^c will be dropped in the sequel for simplicity. In simple shear test, the shear stress τ and mean stress p can be obtained from stress tensor, i.e., $\tau = \tau_{zx}$ and $p = (\sigma_{xx} + \sigma_{yy} + \sigma_{zz})/3$. We will consider the normalized pressure p/p_0 , which is 1 in the initial state, but declines as a result of cyclic shearing. Note that in the soil mechanics literature the quantity $r_u = 1 - p/p_0$, called “excess pore pressure ratio”, is often used to monitor cyclic shearing in the presence of a saturating liquid [19,22,43,44].

The shear strain γ is defined by

$$\gamma = \frac{x_w(t)}{h}, \quad (5)$$

where x_w is the cumulative horizontal displacement of the top wall:

$$x_w(t) = \int_0^t v_x dt. \quad (6)$$

Note that the shear rate $\dot{\gamma}$ is constant and changes its sign only when the shear stress τ reaches the target amplitude τ^{amp} . For this reason, the time interval $T/2$ between two successive

shear reversals varies in different cycles of shearing. Let $T(N)$ be the period of cycle N and t_N its initial time. Since the shear rate is constant, we define a “fractional cycle number” by interpolation between two successive cycles:

$$N' = N + \frac{t - t_N}{T(N)}, \quad (7)$$

where t is the current time. The value of N' coincides with N at $t = t_N$, and increases by one unit at $t = t_N + T$. To avoid confusion, we continue below to use N but in the sense of fractional cycles as defined by N' .

Figure 2 presents the typical macroscopic behavior for simulation T2 of Table I, described in terms of stress path and stress-strain curve, as well as the normalized mean stress evolution and shear strain development as functions of the number of cycles. The simulation starts from $\tau = 0$, $p = p_0 = 100$ kPa, and $\gamma = 0$, corresponding to point A_0 of Fig. 2(a) and the origin of Fig. 2(b). As cyclic shearing continues, the path in the stress space (p, τ) (stress path) oscillates and moves leftwards (decreasing mean stress), indicating an irreversible evolution of the granular microstructure. The “initial liquefaction” occurs when p drops to a residual value close to zero for the first time. The number of cycles required to reach this transition is denoted by N_{IL} shown in Fig. 2. The term “liquefaction” should be understood here as a loss of stability or load-bearing capacity (both the mean and shear stresses),

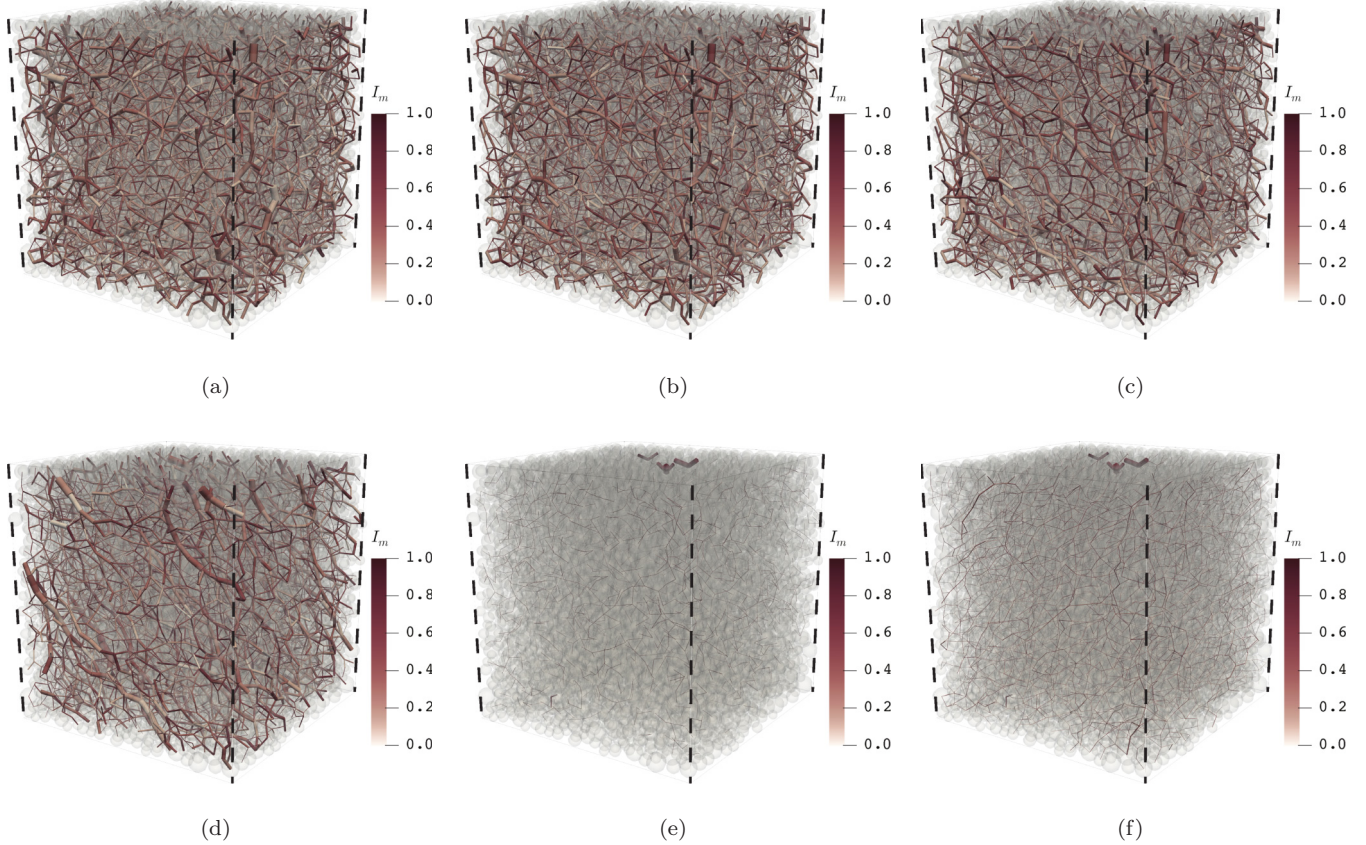


FIG. 3. Snapshot of normal forces in the sheared sample for characteristic state: (a) A_0 ; (b) A_1 ; (c) B_1 ; (d) C_1 ; (e) C_2 ; (f) C_2' . Line thickness is proportional to the normal force at each contact. Color code represents the mobilized friction index I_m (see text) in the range between 0 and 1. The same camera view as Fig. 1 is used here.

and therefore a transition from a solid-like state to a liquid-like state, by analogy with a liquid-saturated load-bearing granular bed where liquefaction occurs by transient load transfer from the contact network to the liquid with the development of excess pore pressure.

Thus, the cyclic shearing process can be divided into pre- and postliquefaction periods, as shown in Fig. 2. Before transition, the shear strain remains negligibly small, as observed in Fig. 2(b). After transition, the stress path gets trapped and oscillates along a butterfly-shaped loop, and shear strain of increasing amplitude develops. The shear strain continues to accumulate in the postliquefaction period and the stress path takes a banana shape. It is important to underline here the cyclic nature of liquefaction in the postliquefaction period. Indeed, during each cycle the shear stress builds up again and the mean stress increases to its highest value until a new strain reversal happens and leads the system to a new liquefaction state. This means that the granular material is dense enough to rebuild partially a force network to sustain shear stresses despite its fragile microstructure prone to collapse by small-amplitude shear stress reversal. In our simulations, the mean stress does not fully vanish, but drops slightly below $p/p_0 \simeq 0.01$. Lower mean stresses are reached at larger void ratios [45].

The features briefly described above are in excellent agreement with well-documented experimental and numerical observations. We will focus below on the particle-level mech-

anisms of liquefaction. Three loading cycles, including cycle A and cycle B in the preliquefaction period, and cycle C in the postliquefaction period, are highlighted in Fig. 2. These cycles are selected to zoom on the detailed evolution of the microstructure in the following. In each cycle, at least four characteristic states are singled out: subscript 0 refers to the first time $\tau \geq 0$, thus distinguishing loading from unloading, subscript 1 refers to the instant where $\tau = \tau^{\text{amp}}$, subscript 2 refers to the first time $\tau < 0$ (reversed shear), and subscript 3 refers to the instant $\tau = -\tau^{\text{amp}}$. In cycle C, two more states are selected, i.e., C_0' and C_2' , both referring to the exit from the liquefaction state.

Figure 3 presents several snapshots of normal force chains at different states of simulation T2 given in Fig. 2. The forces are represented by bars along the branch vectors joining particle centers with their thickness proportional to the intensity of the normal force. The same figure also shows the friction mobilization index I_m at each contact defined by

$$I_m = \frac{|f_t|}{\mu_t f_n}. \quad (8)$$

It varies between 0 and 1 and is displayed in color code. The value $I_m = 1$ corresponds to sliding or fully mobilized friction. Visual inspection reveals several features. First, the initially isotropic force network (A_0) becomes slightly anisotropic at shear stress reaching its maximum amplitude (A_1) and even more anisotropic along loading cycles (B_1

and C_1). Well-connected strong force chains tend to span the system along the first principal stress direction (i.e., compressive direction). Then, upon unloading to liquefaction state (C_2), large force transmission networks are replaced by fragile scattered small force chains [20,46], where normal contact forces drop to much smaller values, and the friction is prone to be mobilized at a large number of contacts, corresponding to an unjammed state [15,46]. Whether the current system is isotropic cannot be inferred from Fig. 3(e). While the sample evolves in the liquefaction state until the exit (C_2'), large deformation accumulates and the collapsed force transmission network is rebuilt. In Fig. 3(f), one can notice that the network nearly percolates along the diagonal from bottom left corner to top right corner (contrary to C_1) in the xz shear plane [see Fig. 1(b)] although the intensity of normal forces is still small. The force network will be further analyzed in the following sections.

IV. GRANULAR MICROSTRUCTURE

In this section, we investigate the evolution of the granular microstructure for the simulation T2 in Table I in terms of particle connectivity, force transmission, and fabric and force anisotropies.

A. Particle connectivity

The lowest-order scalar quantity describing the contact network is the coordination number z_g , defined as the average number of contacts per particle [47]. The coordination number can also approximate the level of static redundancy in the system, i.e., the difference between the total number of constraints and the total number of degrees of freedom. Each contact provides six constraints in an ideal system with infinite tangential, rolling, and torsion friction coefficients. Given six degrees of freedom (dynamic variables) per particle, the critical coordination number, defining the isostatic state with equal numbers of degrees of freedom and constraints, is $z_{iso} = 2$. This is an extremely low value for our system. It will increase if the rolling and twisting interactions are removed. In general, positive and large values of static redundancy $z_g - z_{iso}$ reflect a stable quasistatic behavior, whereas negative values mean unstable and dynamic states. In all cases, there is always a subset of particles with no contacts (floaters) and a subset of contacts bearing no force. Hence, for the definition of the coordination number we consider only the nonfloaters and force-bearing contacts:

$$z_g = \frac{2N_c}{N_p - N_p^0}, \quad (9)$$

where N_p is the total number of particles, N_p^0 is the number of floaters, and N_c is the number of force-bearing contacts.

Figure 4(a) displays the evolution of z_g with the number of cycles N , where the time histories are colored according to the value of p/p_0 . The initial liquefaction (IL) corresponding to $p/p_0 \simeq 0.01$ is marked by a small black circle. We see that z_g decreases on average from its initial value $z_g \simeq 4.76$ with small oscillations during the preliquefaction period and drops below 4.0 while the system tends to its initial liquefaction

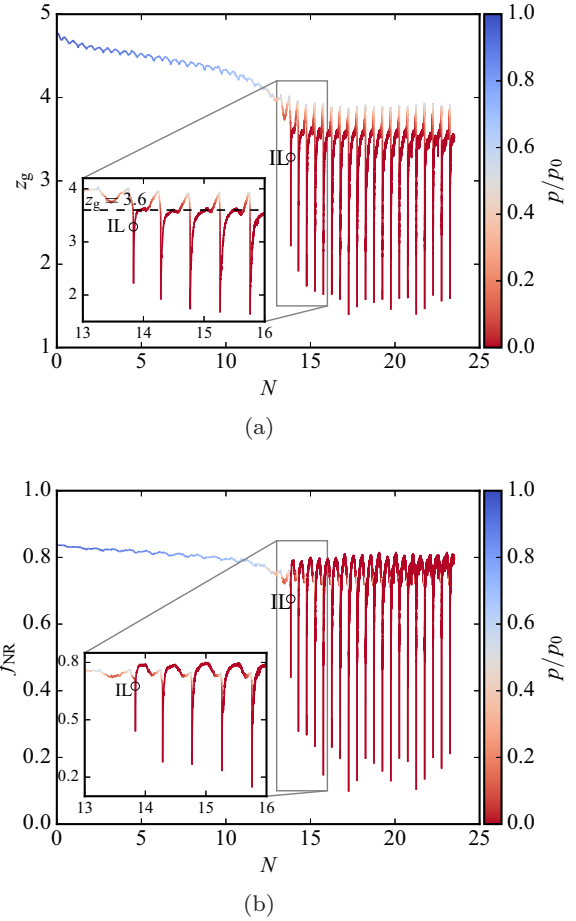


FIG. 4. Evolution of (a) coordination number z_g and (b) non-rattler fraction f_{NR} for simulation T2. The horizontal dashed line $z_g \simeq 3.6$ refers to the inflection point of z_g .

state. After this transition, z_g stays below 4.0 and fluctuates significantly down to values as low as 1.5 with a negative static redundancy, implying that there are not enough constraints to hold the system stable. One can also notice that z_g increases with p/p_0 , implying a monotonic relationship between z_g and p [48,49]. Hence, the coordination number is fully correlated with the evolution of the macroscopic stress and strain parameters during cyclic shearing. Moreover, its lowest nonzero value is consistent with the existence of a residual mean stress. The horizontal dashed line for $z_g = 3.6$ in the inset window corresponds to the inflection point of z_g nearly at mid-distance between two successive cycles. Below this point, z_g increases along with the buildup of the contact network at constant mean stress. Above this value z_g further increases with p and τ (see below). For this reason, the coordination number $z_g \simeq 3.6$ may be considered as the percolation threshold of the particles allowing for force transmission across the system through the contact network and thus transition from fluid-like state to solid-like state.

Another scalar descriptor complementing the coordination number is the “nonrattler fraction” defined by [15]

$$f_{NR} = \frac{N_p - N_p^0 - N_p^1}{N_p}, \quad (10)$$

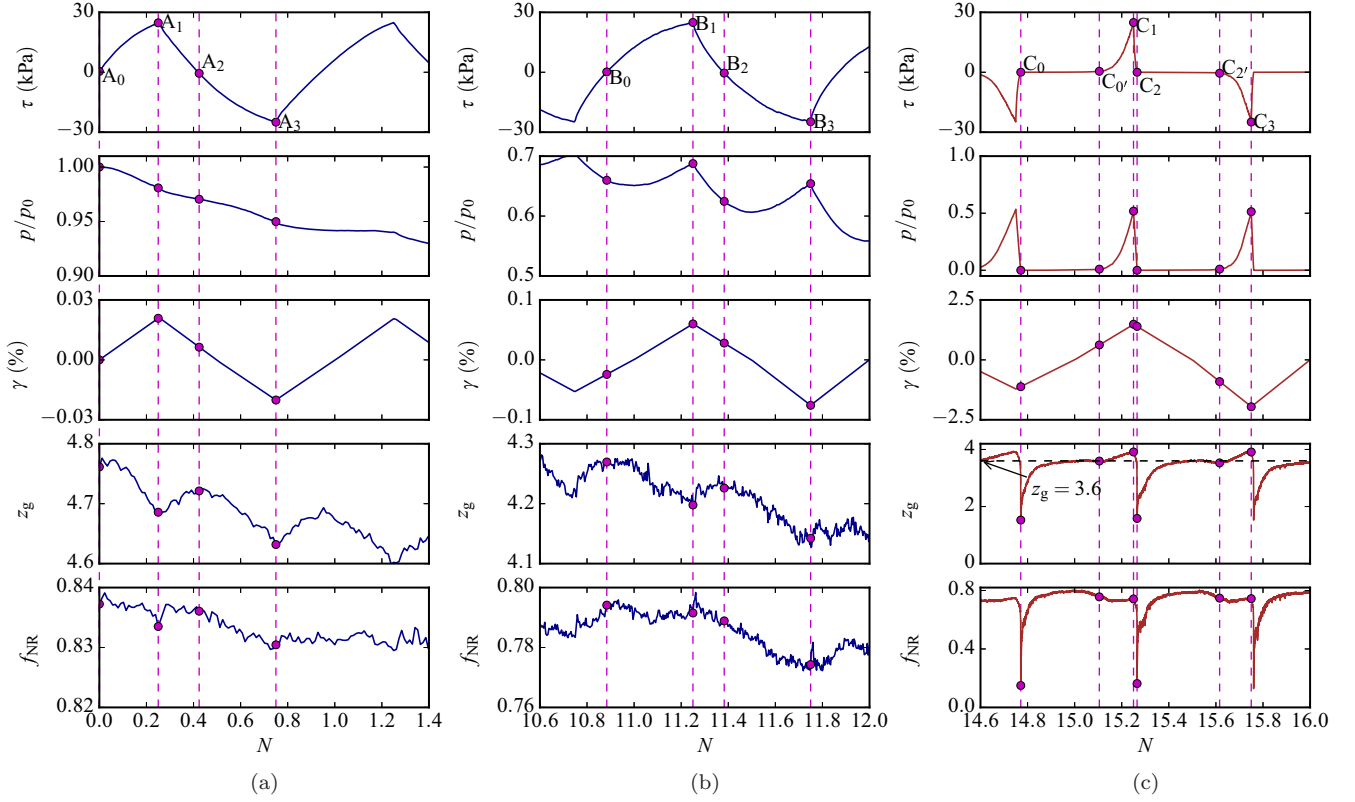


FIG. 5. Detailed evolutions of z_g and f_{NR} , together with those of the shear stress τ , normalized mean stress p/p_0 and shear strain γ , for simulation T2 during three selected cycles: (a) cycle A; (b) cycle B; (c) cycle C.

which represents the proportion of particles with at least two contacts, i.e., excluding particles with zero contact (N_p^0) or one contact (N_p^1). Figure 4(b) shows the evolution of f_{NR} . We see that around 15% of the particles at the initial state do not contribute to the sample's contact network. During the preliquefaction period, f_{NR} gradually declines to 70% at initial liquefaction. In the postliquefaction period, f_{NR} oscillates significantly and drops below 40% transiently when p/p_0 approaches 0, but it does not vanish. It should be noted that the largest values of f_{NR} are achieved as a result of reloading, but before p/p_0 begins to increase, implying that f_{NR} and p do not follow a monotonic relationship.

The above-mentioned features can be observed in Fig. 5, which displays detailed evolution of z_g and f_{NR} in cycles A, B, and C as previously shown in Fig. 2. It is remarkable that in cycle A z_g and f_{NR} oscillate with p/p_0 decreasing monotonically whereas in cycle B they oscillate together with p/p_0 but in opposite phase. Then, in cycle C of the postliquefaction period, the variations of z_g and f_{NR} are directly related to p/p_0 except in the liquefaction state ($p/p_0 \leq 0.01$), as mentioned previously; z_g achieves its local maximum when $\tau = \pm\tau^{\text{amp}}$ while the peak of f_{NR} occurs in the liquefaction state. The horizontal dashed line in the subplot of z_g and N shows that the value $z_g = 3.6$ prompts the system to exit from the liquefaction state, and in this respect it represents the critical value for jamming transition as a percolation threshold of the contact network.

To understand the relationship between p and z_g , let us consider the following relation derived from

Eq. (4):

$$p \propto z_g \frac{N_p - N_p^0}{N_p} \langle \mathbf{l} \cdot \mathbf{f} \rangle = z_g \frac{N_p - N_p^0}{N_p} \langle l f_n \rangle, \quad (11)$$

where $\langle \mathbf{l} \cdot \mathbf{f} \rangle$ refers to the average over all contacts. For the spherical particles used in this study, $\mathbf{l} = l\mathbf{n}$ with l being branch vector length, and thus $\mathbf{l} \cdot \mathbf{f} = l f_n$ with f_n being the contact normal force. In the preliquefaction cycle, the non-floater fraction $(N_p - N_p^0)/N_p$ can be regarded as constant given Figs. 6(a) and 6(b) so that the variation of p is controlled by z_g and $\langle l f_n \rangle$. Hence, the initial out-sync between p/p_0 and z_g is compensated by $\langle l f_n \rangle$, which can be easily affected by cyclic shearing. This compensation becomes less and less significant as the system approaches the initial liquefaction. In the postliquefaction period, f_n becomes negligibly small when the system falls into the liquefaction state, thus explaining why the significant changes of z_g do not affect p noticeably. Outside the liquefaction state, z_g increases mildly, and the increase of p should be mainly attributed to the evolution of $\langle l f_n \rangle$.

To get a more detailed insight into the evolution of the contact network, let us consider the connectivity of particles P_c , defined as the proportion of particles with exactly c contacts. This distribution is shown in Fig. 6 at the characteristic states of the three selected cycles. Note that P_0 represents the proportion of floating particles. In the preliquefaction cycles, the distribution $\{P_c\}$ is nearly unchanged during shear cycle with very small values of P_1 and P_2 , a peak at $c = 4$, and a

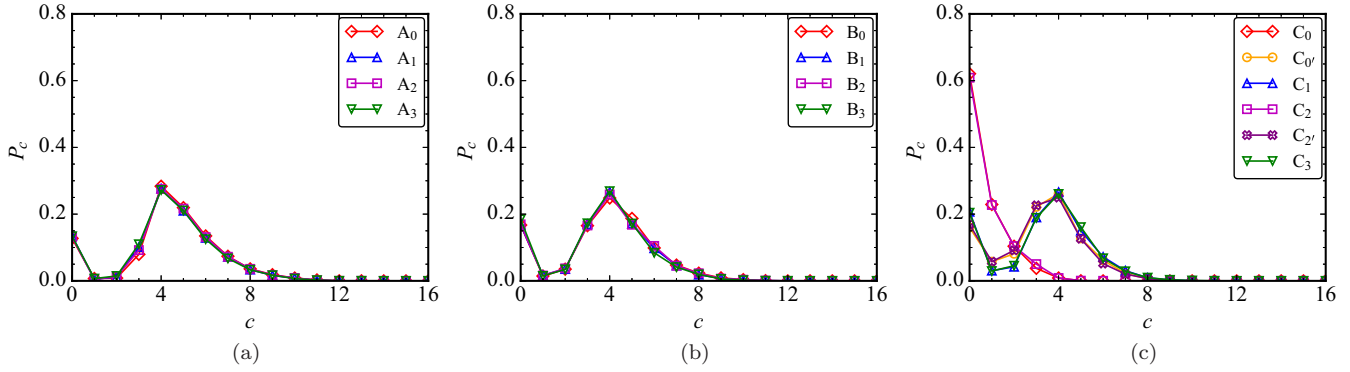


FIG. 6. Connectivity diagram expressing the fractions P_c of particles with exactly c contacts for simulation T2 at the characteristic states of (a) cycle A; (b) cycle B; (c) cycle C.

long tail for $c > 4$. In cycle C of the postliquefaction period, the states C_0 and C_2 exhibit a high proportion of particles with $c < 4$, implying a fragile contact network. This fragile network disappears only when the system exits the liquefaction state as shown by $\{P_c\}$ at C_0' and C_2' . Given large shear strain development between C_0 and C_0' or C_2 and C_2' , one can infer that sample deformation rebuilds the fragile network resulting from unloading (compare C_1 and C_2) although p does not increase markedly. The system stays stable at C_1 or C_3 while C_0 or C_2 represents the state with the weakest contact network in the postliquefaction cycle.

For the temporal evolution of P_c , we plot in Fig. 7 P_c for $c = 0, 1, \dots, 9$ at $\tau = \tau^{\text{amp}}$ and $\tau \simeq 0$ (transitioning from unloading to loading) as a function of N . $\tau \simeq 0$ refers to C_2 in the postliquefaction period. At $\tau = \tau^{\text{amp}}$, we observe that the proportion of floaters (P_0) takes the place of P_5 to become the second most dominant value after a few cycles while P_4 does not change noticeably. At $\tau \simeq 0$, near initial liquefaction ($N \simeq 14$), a significant change occurs in the connectivity diagram: the system tends to have more proportions of particles with contacts below 3. In the postliquefaction period, the values of P_0, P_1 and P_2 first increase, implying that the system gets weaker, and explaining the increasing shear strain amplitude, and then tends to a steady state. Furthermore, in the postliquefaction period, the distribution $\{P_c\}$ is continuous between floaters (P_0) and the nonfloaters, and the peak at $c = 4$ has disappeared. This means that $\{P_c\}$ does not anymore reflect a balanced contact network but a dynamic one in which dynamic events such as binary collisions (P_1) and unstable chains (P_2) of particles prevail.

B. Force transmission and friction mobilization

The force network of a granular system is defined by the spatial distribution of contact forces f . A local coordinate system (\mathbf{n}, \mathbf{t}) is attached to each contact point, where \mathbf{n} is the unit vector perpendicular to the contact plane and \mathbf{t} is an orthonormal unit vector in the contact plane oriented along the tangential contact force. Thus, we have $\mathbf{f} = f_n \mathbf{n} + f_t \mathbf{t}$, with f_n and f_t representing the magnitudes of normal and tangential contact forces, respectively. The inhomogeneity of contact forces in granular media can be characterized by the probability density function (PDF) of normal contact forces P_n [50,51], which is generally characterized by two major features: (1) the

PDF is roughly a decreasing exponential function for forces above the mean, and (2) in the range of weak forces below the mean the PDF does not decline to zero with force. These two features have been observed in confined packings [50,52] or sheared granular media reaching steady flow regime [53–55] where the system preserves a statistically stable force distribution. For the granular assembly under isochoric cyclic

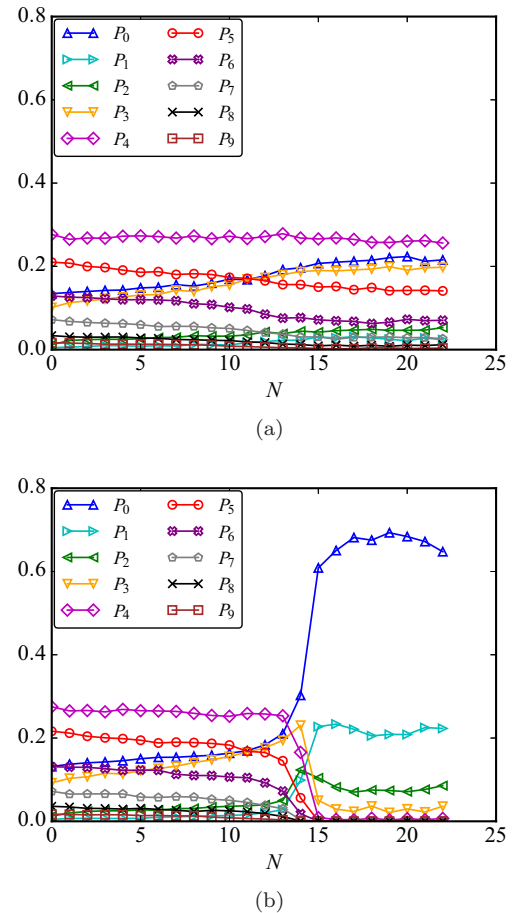


FIG. 7. Evolution of proportion P_c of particles with c contacts at characteristic states of (a) $\tau = \tau^{\text{amp}}$ and (b) $\tau \simeq 0$ transitioning from unloading to loading (or C_2 in postliquefaction period) for simulation T2.

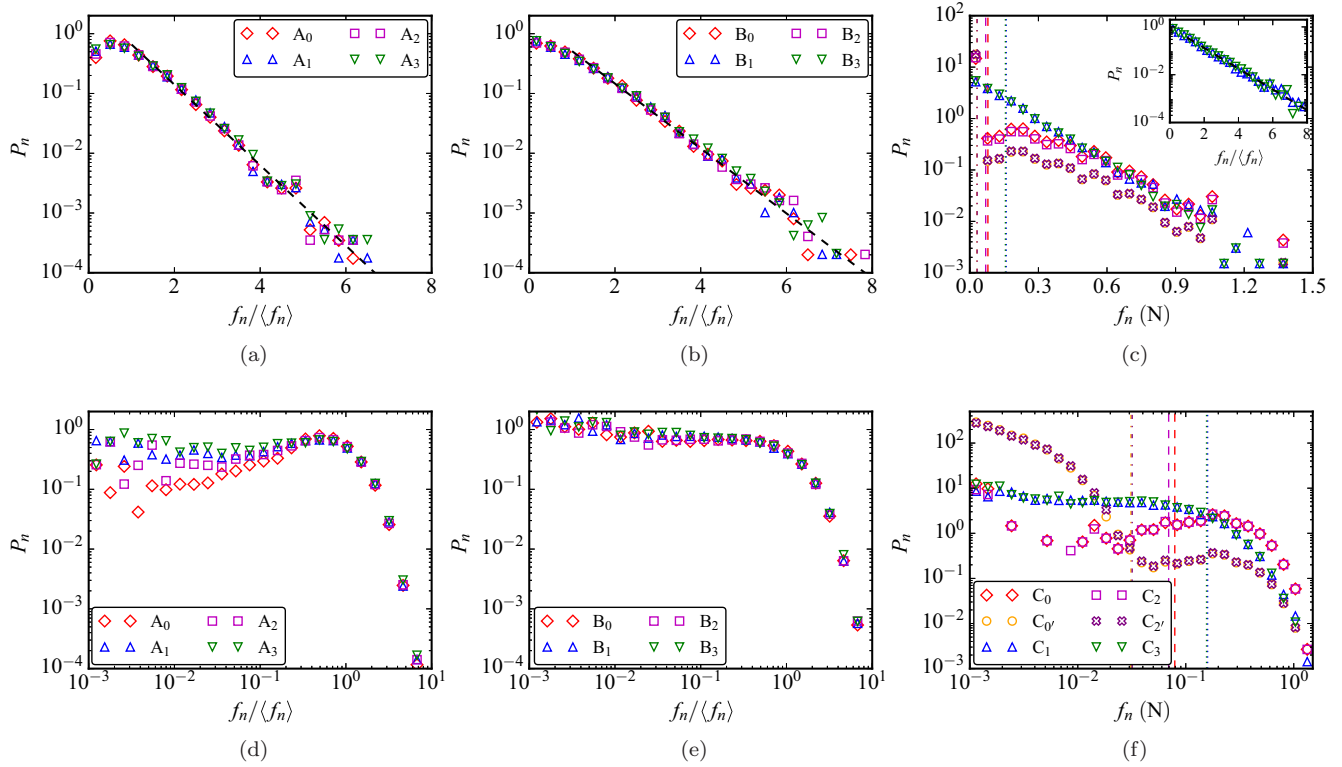


FIG. 8. Probability density functions P_n of normal forces f_n normalized by the mean normal force in log-linear [(a), (b), (c)], and log-log scales [(d), (e), (f)] for simulation T2 at characteristic states of cycle A [(a), (d)]; cycle B [(b), (e)]; cycle C [(c), (f)]. Note that plots for cycle C share the legend, and the vertical dash-dotted, dashed, and dotted lines there refer to $\langle f_n \rangle$ at $C_{0'}$ or $C_{2'}$, C_0 or C_2 , and C_1 or C_3 , respectively.

shearing, the network goes through collapsing and jamming stages, and therefore we expect strong variations of P_n .

Figure 8 displays the PDF of normal contact forces in log-linear and log-log scales at the characteristic states depicted in Fig. 2. In the preliquefaction cycles, the forces are normalized by the mean normal contact force $\langle f_n \rangle$ at each state given the tiny variations of $\langle f_n \rangle$ in a cycle. In the postliquefaction cycles, $\langle f_n \rangle$ changes significantly. For example, $\langle f_n \rangle \simeq 0.16$ N at C_1 and 0.03 N at $C_{2'}$, as shown by the vertical dashed lines in Figs. 8(c) and 8(f). Thus, to see the variations of force PDF in the postliquefaction period, it is more suitable not to normalize f_n any more, as depicted in Figs. 8(c) and 8(f). We see that P_n is well fitted by a decreasing exponential function $ke^{\beta(1-f_n/\langle f_n \rangle)}$ for $f_n \geq \langle f_n \rangle$ where k and β are two parameters [56] representing the value of P_n at $f_n = \langle f_n \rangle$ and the slope of the log-linear plots in Fig. 8, respectively. We find $\beta \simeq 1.55$ in cycle A, 1.25 in cycle B, and 1.00 in cycle C at C_1 and C_3 . This means that the force network is increasingly more inhomogeneous as it evolves from cycle A to cycle B and then cycle C. Upon entering the liquefaction state (C_0 or C_2), the system has a slightly larger proportion of strong forces than C_1 or C_3 as shown in Figs. 8(c) and 8(f). However, the proportion of strong forces becomes smaller than C_1 or C_3 when the system leaves the liquefaction state and jamming transition occurs ($C_{0'}$ and $C_{2'}$).

The distribution of tangential contact forces in the system can be analyzed in a similar way [50,51]. In addition, one can also link each tangential contact force to the friction mobilization, as given by the friction mobilization index $I_m = |f_t|/(\mu_c f_n)$ [51,55,57]. This index ranges between 0 and 1, the

latter indicating sliding or mobilized contact. Generally, the proportion of mobilized contacts is expected to increase with shear stress [41]. This is confirmed in Fig. 9 by comparing states of subscript 0 or 2 with those with subscripts 1 or 3 in preliquefaction cycles.

We also observe a right shift of the distribution of I_m , indicating a larger proportion of contacts getting close to sliding. In the postliquefaction period, a large proportion of mobilized contacts is generated at C_0 and C_2 : the probability density near $I_m = 1.0$ increases from 0.6 to 14.7. With shear strain developing in the liquefaction state from C_0 to $C_{0'}$ or C_2 to $C_{2'}$, the proportion of mobilized contacts drops to around 0.3, and the system regains larger number of contacts far from sliding. It should be noted that the distribution of I_m at $\tau = \pm\tau^{\text{amp}}$ is nearly the same for the cycles A, B, and C, implying a close relation between friction mobilization and the stress state τ^{amp} .

C. Fabric and force anisotropies

By analyzing the distribution of directional data in the system, a list of higher-order tensorial quantities such as fabric and force tensors can be introduced [58]. These directional data include contact normals \mathbf{n} , mean branch vectors $\langle l \rangle(\mathbf{n})$, mean normal and tangential forces denoted by $\langle f_n \rangle(\mathbf{n})$ and $\langle f_t \rangle(\mathbf{n})$, to name a few. Given the low polydispersity of samples in this study, the fabric anisotropy due to $\langle l \rangle(\mathbf{n})$ is nearly negligible and will not be analyzed here.

Let us consider $S(\mathbf{n})$, the set of contact normal vectors pointing in the direction $\mathbf{n} = (\theta, \varphi)$ as shown in Fig. 10, where

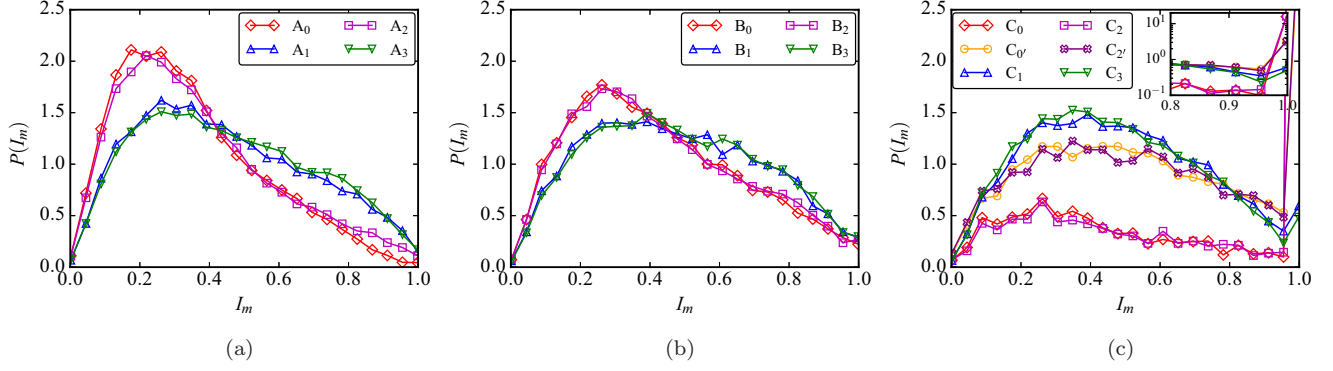


FIG. 9. Probability density functions of friction mobilization index for simulation T2 at characteristic states of (a) cycle A; (b) cycle B; (c) cycle C.

θ is the angle of contact normal vector projected on the shear plane, i.e., xz plane in Fig. 10, and φ the azimuthal angle. The PDF of contact normals, and the average normal and tangential forces are expressed as functions of the orientation \mathbf{n} [55,59]:

$$P(\mathbf{n}) = \frac{N_c(\mathbf{n})}{N_c}, \quad (12)$$

$$\langle f_n \rangle(\mathbf{n}) = \frac{1}{N_c(\mathbf{n})} \sum_{c \in \mathcal{S}(\mathbf{n})} f_n, \quad (13)$$

$$\langle f_t \rangle(\mathbf{n}) = \frac{1}{N_c(\mathbf{n})} \sum_{c \in \mathcal{S}(\mathbf{n})} f_t, \quad (14)$$

where $N_c(\mathbf{n})$ is the number of contacts pointing in the direction \mathbf{n} within a small solid angle $\delta\Omega$ around \mathbf{n} .

Given the invariance of simple shear loading along the y axis, we expect that the distributions do not depend on the azimuthal angle, and hence we consider only the projections of contact orientations on the shear plane. Thus, contact normal \mathbf{n} is replaced by the vector \mathbf{n}' on the shear plane with orientation angle θ as shown in Fig. 10 and the unit vector \mathbf{t} representing the direction of corresponding tangential force is replaced by

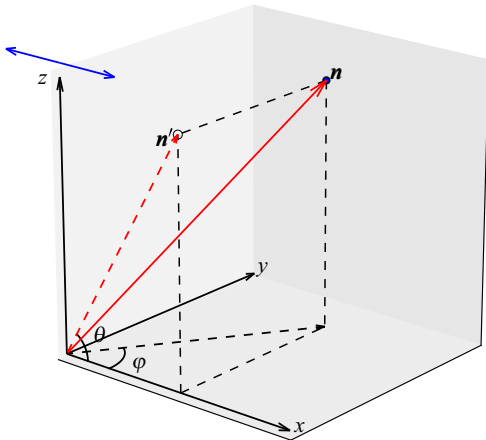


FIG. 10. Normal contact orientation given the azimuthal angle φ and the angle θ defined by the projection of the contact direction on the shear plane of xz . The double-headed arrow represents the cyclic shear direction.

the vector \mathbf{t}' on the shear plane with orientation angle $\theta + 90^\circ$, perpendicular to \mathbf{n}' .

Figure 11 displays the polar representation of the functions $P(\mathbf{n})$, $\langle f_n \rangle(\mathbf{n})$ and $\langle f_t \rangle(\mathbf{n})$ in shear plane as a function of θ at the characteristic states. We observe an obviously anisotropic behavior when the shear stress reaches the peak: for $P_n(\theta)$ and $\langle f_n \rangle(\theta)$, the major principal components occur in the direction $\theta \simeq 135^\circ$; for $\langle f_t \rangle(\theta)$ it occurs at $\theta \simeq 90^\circ$, and the other peak at $\theta \simeq 45^\circ$ corresponds to the minor principal component where $\langle f_t \rangle(\theta) < 0$. The directions for the peaks of $\langle f_n \rangle(\theta)$ and $\langle f_t \rangle(\theta)$ can be approximated by the directions of planes with major principal stress and maximum shear stress, respectively. By drawing a Mohr circle, one can see that the angle between these two directions is 45° , which is verified in Figs. 11(b) and 11(c). Comparing the anisotropies of A_1 , B_1 , and C_1 , one can notice an increasing trend for $P_n(\theta)$, a shrinking trend for $\langle f_n \rangle(\theta)$ due to the decrease of p , and a decreasing trend for $\langle f_t \rangle(\theta)$, as elucidated quantitatively below. When the shear stress vanishes (A_0) in the preliquefaction period, the system tends to be isotropic, but it becomes anisotropic in the postliquefaction period except for $\langle f_t \rangle(\theta)$ (consistent with low values of friction mobilization I_m as discussed previously). From C_2 to C_2' , one observes that the fabric anisotropy is regained prior to the force anisotropies, as generally observed during shear reversal [29].

To account for the lowest-order anisotropy of $P(\mathbf{n})$, a second-order fabric tensor can be defined as [60,61]

$$\phi_c = \frac{1}{N_c} \sum_{c \in N_c} \mathbf{n}^c \otimes \mathbf{n}^c, \quad (15)$$

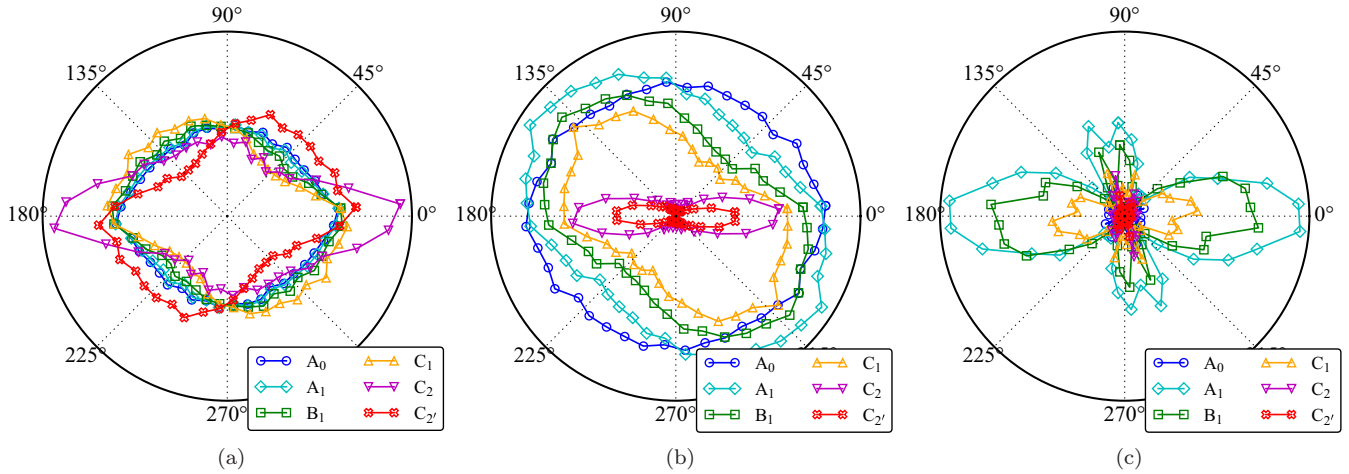
from which the fabric anisotropy tensor \mathbf{a}_c can be defined by

$$\mathbf{a}_c = \frac{15}{2} (\phi_c - \frac{1}{3} \mathbf{I}), \quad (16)$$

where \mathbf{I} is the second-order identity tensor. One can refer to Ref. [58] for details of derivation. In the same way, force tensors characterizing the second-order anisotropy of $\langle f_n \rangle(\mathbf{n})$ and $\langle f_t \rangle(\mathbf{n})$ are defined by the following weighted fabric tensors:

$$\phi_n = \frac{1}{N_c} \sum_{k \in N_c} \frac{f_n^k \mathbf{n}^k \otimes \mathbf{n}^k}{1 + \mathbf{a}_c : (\mathbf{n}^k \otimes \mathbf{n}^k)}, \quad (17)$$

$$\phi_t = \frac{1}{N_c} \sum_{k \in N_c} \frac{f_t^k \otimes \mathbf{n}^k}{1 + \mathbf{a}_c : (\mathbf{n}^k \otimes \mathbf{n}^k)}. \quad (18)$$


 FIG. 11. Polar representation of the functions (a) $P_n(\theta)$, (b) $\langle f_n \rangle(\theta)$ and (c) $\langle f_t \rangle(\theta)$ at selected characteristic states for simulation T2.

Hence, the force anisotropy tensors are given by [23,62]

$$\mathbf{a}_n = \frac{15}{2} \left[\frac{\boldsymbol{\phi}_n}{\text{tr}(\boldsymbol{\phi}_n)} - \frac{1}{3} \mathbf{I} \right], \quad (19)$$

$$\mathbf{a}_t = \frac{15}{3} \frac{\boldsymbol{\phi}_t}{\text{tr}(\boldsymbol{\phi}_n)}, \quad (20)$$

where $\text{tr}(\cdot)$ is the trace operator. Eq. (18) implies that $\text{tr}(\boldsymbol{\phi}_t) = 0$ given the normality of \mathbf{n} and \mathbf{t} .

We use the deviatoric invariants of the anisotropy tensors to quantify the anisotropies of the contact network, normal forces, and tangential forces [41]:

$$a_{[\]} = \text{sgn}(S_{[\]}) \sqrt{\frac{3}{2} \mathbf{a}_{[\]} : \mathbf{a}_{[\]}}, \quad (21)$$

where the subscript $[\]$ stands from c , n , or t , corresponding to the three aforementioned anisotropies, respectively. $S_{[\]}$ is the normalized first joint invariant between two tensors defined by

$$S_{[\]} = \frac{\mathbf{a}_{[\]} : \mathbf{s}}{\sqrt{\mathbf{a}_{[\]} : \mathbf{a}_{[\]}} \sqrt{\mathbf{s} : \mathbf{s}}}, \quad (22)$$

where $\mathbf{s} = \boldsymbol{\sigma} - p\mathbf{I}$ and the deviatoric stress $q = \sqrt{(3/2)\mathbf{s} : \mathbf{s}}$. Generally $S_{[\]}$ quantifies the level of proportionality between two tensors, with $S_{[\]} = 1.0$ corresponding to the proportionality of two tensors. As these anisotropy tensors are affected by \mathbf{s} , $S_{[\]}$ can be regarded as characterizing the relative orientation of the principal axes (PA) of $\mathbf{a}_{[\]}$ with respect to that of \mathbf{s} , i.e., the level of coaxiality.

The fabric and force anisotropies are the origins of shear strength in granular materials [62,63] as s/p can be well approximated by a linear combination of the anisotropy tensors:

$$\frac{\boldsymbol{\sigma}'}{p} \simeq \frac{2}{5} \left(\mathbf{a}_c + \mathbf{a}_n + \frac{3}{2} \mathbf{a}_t \right). \quad (23)$$

At $\tau = \pm\tau^{\text{amp}}$, these anisotropy tensors become nearly proportional to \mathbf{s} . Thus Eq. (23) can be further simplified to

$$\frac{q}{p} \simeq \frac{2}{5} \left(a_c + a_n + \frac{3}{2} a_t \right). \quad (24)$$

Equation (24) holds quite well for our data in Fig. 12 in which the evolutions of fabric and force anisotropies at $\tau =$

$\pm\tau^{\text{amp}}$ are shown along with the contributing weight of each anisotropy to q/p . It should be noted that these anisotropies are normalized by $(2/5)a_c + (2/5)a_n + (3/5)a_t$. We see that a_c and a_n present an increasing trend while a_t decreases slowly in the preliquefaction period. All the anisotropies tend to level off after several cycles in the postliquefaction period, where the normal force anisotropy and contact anisotropy govern the shear force-transmitting network, and friction mobilization or tangential force anisotropy play a marginal role. This is consistent with dense inertial granular flows, where it was shown that the contact anisotropy increases with the inertial number [64]. In this sense, the larger values of the inertial number in the postliquefaction period (although strongly varying during each cycle) may explain the larger level of q/p and the marginal role of tangential force anisotropy.

The contact network anisotropy a_c provides the geometrical support of the stress anisotropy. Its contribution reflects the larger number of contacts oriented along the compression direction (principal direction of the strain-rate tensor) compared with that along the extension direction. This means that there are more contacts to support the forces along the major principal stress direction than the minor principal stress direction. In a dense system, the buildup of the contact anisotropy implies the loss of contacts along the extension direction. This is consistent with the increase in the number of particles with fewer than 4 contacts, as observed in Fig. 6. The normal force anisotropy a_n means that stronger force chains are formed along the major principal stress direction as compared to the minor principal direction. This, in turn, implies an increase in the number of weak forces, as observed in the PDF of normal forces in Fig. 8. The tangential force anisotropy a_t represents the largest friction mobilization occurring in the shear plane. Indeed, the polar diagram of the average tangential force in Fig. 11(c) can be approximated by a truncated Fourier expansion $\langle f_t \rangle(\theta) = a_t \langle f_n \rangle \sin 2(\theta - \pi/4)$. Hence, the friction mobilization index $I_m = \langle f_t \rangle / (\mu_t \langle f_n \rangle) = a_t / \mu_t$ is proportional to the tangential force anisotropy $\theta = 0$ or $\pi/2$. In the postliquefaction period, not only the anisotropies but also the force distributions, friction mobilization distribution, and connectivity function are

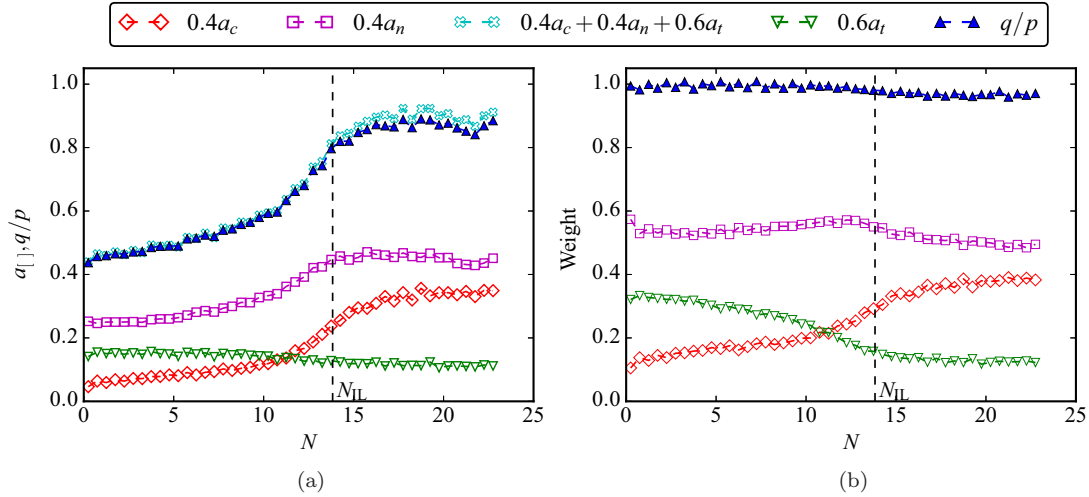


FIG. 12. (a) Evolutions of the contact and force anisotropies at $\tau = \pm\tau^{\text{amp}}$ for simulation T2 and deviatoric stress ratio q/p both measured from the simulation data and expressed as a function of the anisotropies as in Eq. (24). (b) Contributing weights of fabric and force anisotropies to the deviatoric stress ratio q/p : all normalized by $(2/5)a_c + (2/5)a_n + (3/5)a_t$.

nearly stable, as shown in Fig. 13 at $\tau = \pm\tau^{\text{amp}}$ in the last few cycles of the simulation.

Figure 14 displays the evolutions of $S_{[]}$ and anisotropies in the selected three cycles, along with the measured values of q/p and τ/p according to Eq. (4) and predicted values suggested by Eqs. (24) and (23), respectively. From the quick adjustment of S_n and S_t , one can realize that the force anisotropies are easily affected by cyclic shearing while the fabric anisotropy needs more time for the gain of new contacts along a new direction when the shear direction is reversed. In the liquefaction state of Fig. 14(c) (C_0 to C_0' or C_2 to C_2'), all the anisotropies present fluctuations, implying a state with local instabilities. Then, a_c starts to build up and grows into a force-bearing network. This evolution is marked by the increase of a_c and decrease of a_t . Hence, a distinctive feature of the rejammed states (from C_0' to C_1 or from C_2' to C_3) in the postliquefaction period is that the normal force anisotropy prevails and the contact anisotropy is above the tangential force anisotropy. In the preliquefaction state the tangential force anisotropy is mostly above the contact anisotropy, which has generally a low value.

It is noteworthy to remark that, although q and p have small values in the liquefaction state of cycle C, their ratio q/p has reasonable values with variations between 0 (upon shear reversal) and 0.8 after the percolation of the contact network (C_0'). The latter is above the maximum values of q/p reached in cycles A and B, and reflects the fact that the states reached at jamming in the postliquefaction period are different from the preliquefaction states even though in both cases the granular material is shear-jammed. This is obviously related to the higher contact and force anisotropies that can be reached in the postliquefaction state. In the preliquefaction period, the predicted quantities from Eqs. (24) and (23) agree well with the measured values, despite a slight loss of accuracy upon unloading for the predicted q/p due to noncoaxiality between the stress tensor and anisotropy tensors during transient reversal. This inaccuracy is also present in the liquefaction state of the postliquefaction period where q , p and τ have quite small values [29].

Figure 15 presents the fabric anisotropy a_c versus the coordination number z_g during the cyclic shearing process. The evolution of the system in the fabric space (z_g, a_c) portrays the

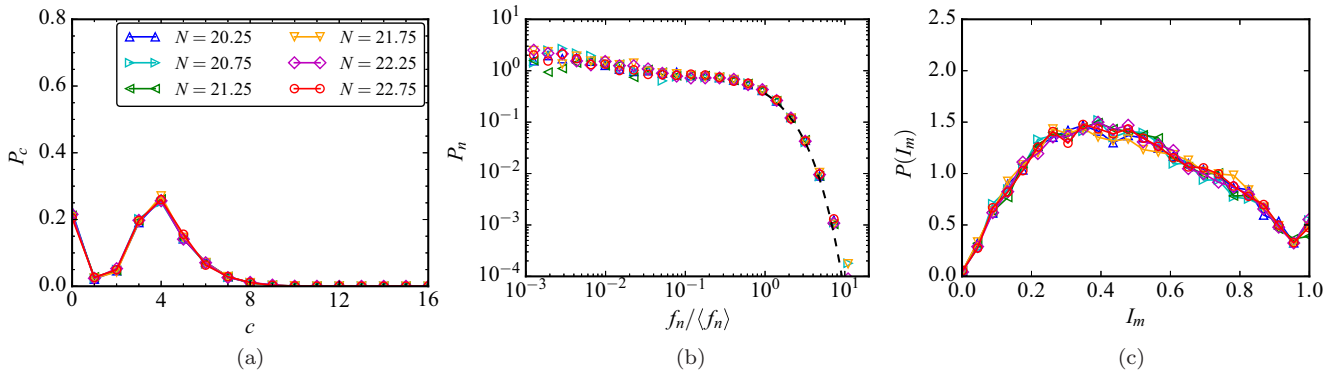


FIG. 13. Snapshots of (a) particle connectivity diagram, probability density functions of (b) normal forces and (c) mobilized friction index when shear stress reaches its maximum amplitude in the last three cycles of simulation T2.

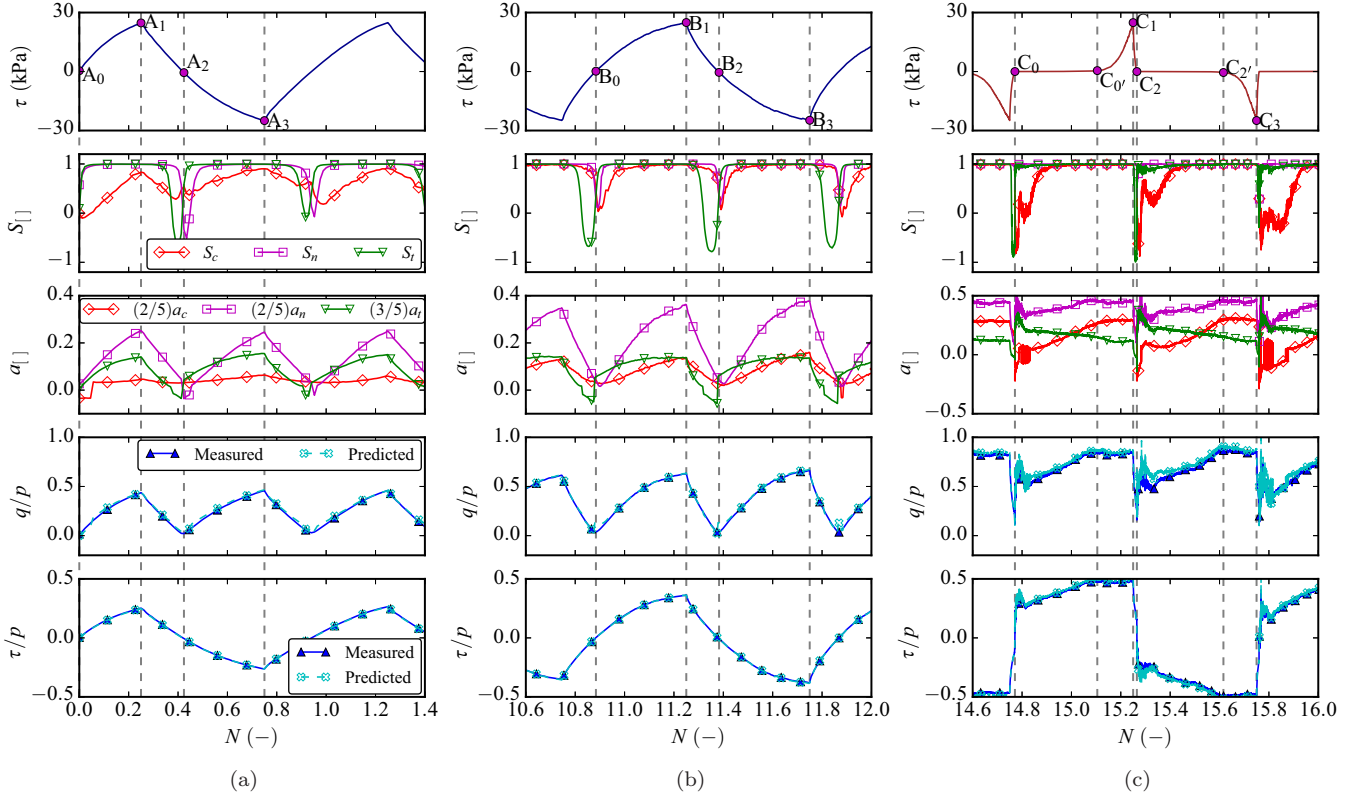


FIG. 14. Evolutions of $S_{||}$ and anisotropies, along with comparisons between calculated q/p and τ/p and their predicted values by Eqs. (24) and (23) for simulation T2: (a) cycle A; (b) cycle B; (c) cycle C.

reorganizations of the contact network in response to external loading [65]. The negative values of a_c correspond to the states where S_c is negative, i.e., the principal directions of the stress tensor and fabric anisotropy tensor make an angle larger than $\pi/4$. The instances of shear stress change of sign, i.e., the states with subscripts 0 and 2 in each cycle, are marked by the diamond symbols. The instances of peak shear stress, i.e., the states with subscripts 1 and 3 in each cycle,

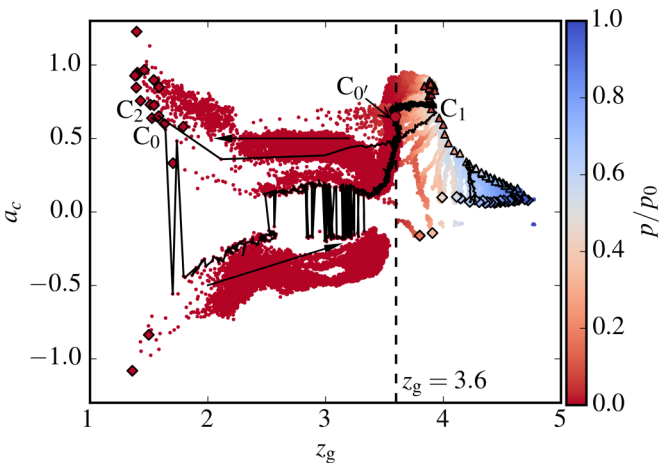


FIG. 15. Fabric anisotropy a_c versus coordination number z_g during the cyclic shearing for simulation T2. The colors represent the stress level according to the color scale. The highlighted path is a full shear cycle in the postliquefaction period.

are marked by triangles. The states from C_0 to C_2 of cycle C are interconnected to reveal the fabric evolution path in the postliquefaction period, with characteristic states highlighted.

On the right side of the fabric diagram beyond $z_g > 3.6$ in the preliquefaction period, the evolution of the system starts from $a_c \simeq 0$ and high value of z_g (where $\tau \simeq 0$), and follows a path towards the left (lower values of z_g) via oscillations between $a_c = 0$ and a maximum value of a_c that increases gradually with the number of cycles. The upper limit of a_c defines a decreasing function of z_g , which was termed “gain saturation line” in Ref. [65] since for large values of z_g no more contacts can be gained along the direction of contraction. The steric exclusions restrict the number of contacts that can be gained, and thus the value of the fabric anisotropy. A simple model predicts that the maximum value of fabric anisotropy varies as $1/z_g$ in agreement with our data points in Fig. 15. Interestingly, the largest value of fabric anisotropy occurs around $z_g \simeq 3.6$ with $a_c \simeq 0.9$, where the initial liquefaction occurs.

In the postliquefaction period, both z_g and a_c vary significantly and follow long paths exemplified by that from C_0 to C_0' . In particular, we observe a plateau along which a_c is nearly constant while z_g either increases or declines. This means that along this plateau, the contacts are lost or gained isotropically. We see that after the system gets out of liquefaction state, a_c does not change noticeably from C_0' to C_1 despite the increase of the applied shear stress τ . Upon unloading from C_1 to C_2 , z_g drops significantly while a_c does not change noticeably. At low values of z_g , a larger anisotropy is reached by loss of contacts along the direction of extension.

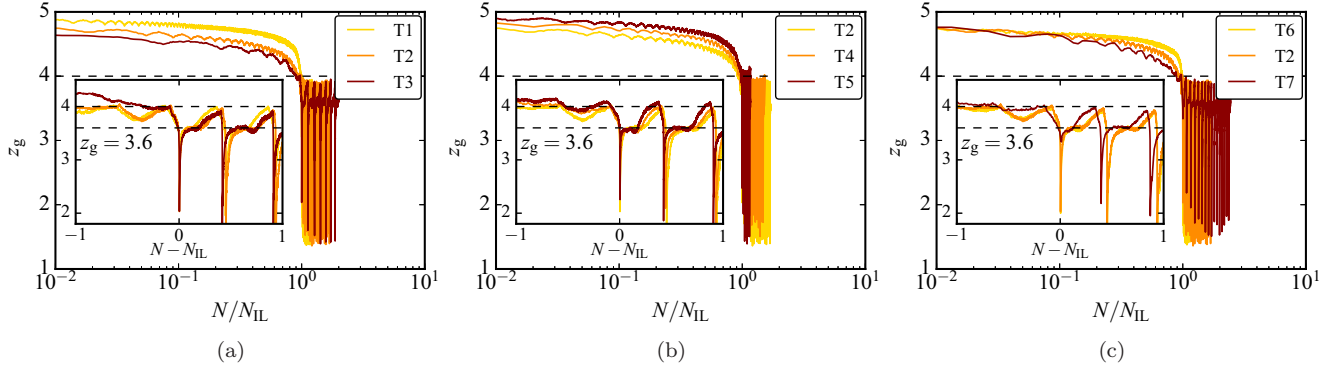


FIG. 16. Effects of (a) initial void ratio e , (b) initial mean stress p_0 and (c) cyclic stress ratio (CSR) on the evolution of coordination number z_g .

But the anisotropy is limited by “loss saturation.” Indeed, the particles’ relative stability impedes the loss of all contacts along the direction of extension. However, due to the shear deformation of the sample, the contact network is rebuilt by first isotropic and then anisotropic gain of contacts with steady increase of both z_g and a_c . The largest value of a_c achieved along this path is above 1 in the unjammed state, in agreement with Ref. [24], and 0.75 in the jammed state. This anisotropy occurs for $z_g \simeq 4$. Along this path of rejamming, we observe also frequent changes of the sign of a_c due to the rotations of its direction with respect to that of the stress tensor. As the contact network can not easily change its orientation, these rotations arise from the rotations of the stress tensor with weak shear components (small values of both p and τ). We see that in the postliquefaction period the anisotropy almost never vanishes whereas in the preliquefaction period, declines to a value close to zero after each shear reversal.

V. EFFECTS OF INITIAL AND LOADING CONDITIONS

This section extends our study to the other simulations listed in Table I to explore the effects of initial and loading conditions on the evolution of microstructure. Simulations T1, T2, and T3 are used to analyze the effect of the initial void ratio e_0 . Simulations T2, T4, and T5 are used to analyze the effect of the initial mean stress p_0 . Simulations T6, T2, and T7 are used to analyze the effect of CSR defined by Eq. (3).

Figure 16 displays the evolution of z_g for all the simulations listed in Table I. We normalize the number of cycles N by N_{IL} , thus the vertical line $N/N_{IL} = 1$ distinguishes the preliquefaction period from the postliquefaction period. In the inset window of each figure, the x axis is replaced by $(N - N_{IL})$ to zoom into the details near the initial liquefaction. We see that the evolution of the coordination number in all simulations is quite similar to that of T2. Recall that, as observed in Fig. 4(a), z_g stays below 4.0 in the postliquefaction period, but this is not the case for simulation T5 in Fig. 16(b) where the mean stress corresponding to $\tau = \pm\tau^{\text{amp}}$ in the postliquefaction period is expected to be around six times that of simulation T2. Given the monotonic relationship between z_g and p [49,66] indicated by Eq. (11), it is reasonable that z_g evolves beyond 4.0 in the postliquefaction period for a simulation inducing a high postliquefaction mean stress. Given the sudden drop

of z_g upon unloading in each postliquefaction cycle, it is difficult to find the value corresponding to transition to the liquefaction state. As indicated by Fig. 16, z_g stays above 3.6 in the preliquefaction period. Hence, the value $z_g = 3.6$ seems to control the transition to the liquefaction state independently of e_0 , p_0 , and CSR. This is consistent with the interpretation of 3.6 as the mechanical threshold for jamming or percolation threshold for contact network. However, the lowest values of z_g reached after shear reversal seem to slightly depend on the void ratio and cyclic stress ratio although a broader range of the values of these parameters should be simulated for a quantitative evaluation of these effects.

Figure 17 shows the evolution of the respective contributions of the fabric and force anisotropies to the deviatoric stress ratio q/p at $\tau = \pm\tau^{\text{amp}}$ for the simulations of Table I except T2. The theoretical value of q/p calculated from the anisotropies by Eq. (24) is shown, too. We see that the effect of the initial and loading conditions on the evolution patterns is not significant. In all cases, the contribution of a_t is larger than that of a_c in the preliquefaction period, but their roles interchange during the postliquefaction period. The marginal contribution of a_t in the postliquefaction period is consistent with previous simulations [23]. The larger contribution of a_c in the postliquefaction period reflects the higher mobility and lower coordination number of the particles allowing larger fabric anisotropy. The higher mobility also involves a lower degree of frustration of particle rotations and thus lower friction mobilization, which is at the origin of tangential anisotropy.

Despite their similarity, one can observe some differences in the first few loading cycles, but cyclic shearing reduces these initial differences in the subsequent cycles. After a sufficient number of cycles in the postliquefaction period, the contribution of $(2/5)a_c$ saturates at around 0.4, that of $(2/5)a_n$ saturates at around 0.5, and the rest is attributed to $(3/5)a_t$. In the postliquefaction period, the stress path falls into the banana shape, implying a constant deviatoric stress ratio q/p during loading outside the liquefaction state [refer to the period between C_0 and C_1 in Fig. 14(c)]. The system can quickly adjust itself to support the shear stress amplitude by properly allocating each anisotropy weight. Figure 18 displays the particle connectivity diagram, probability density functions of normal forces and mobilized friction index at the last time the shear stress reaches the maximum amplitude in each

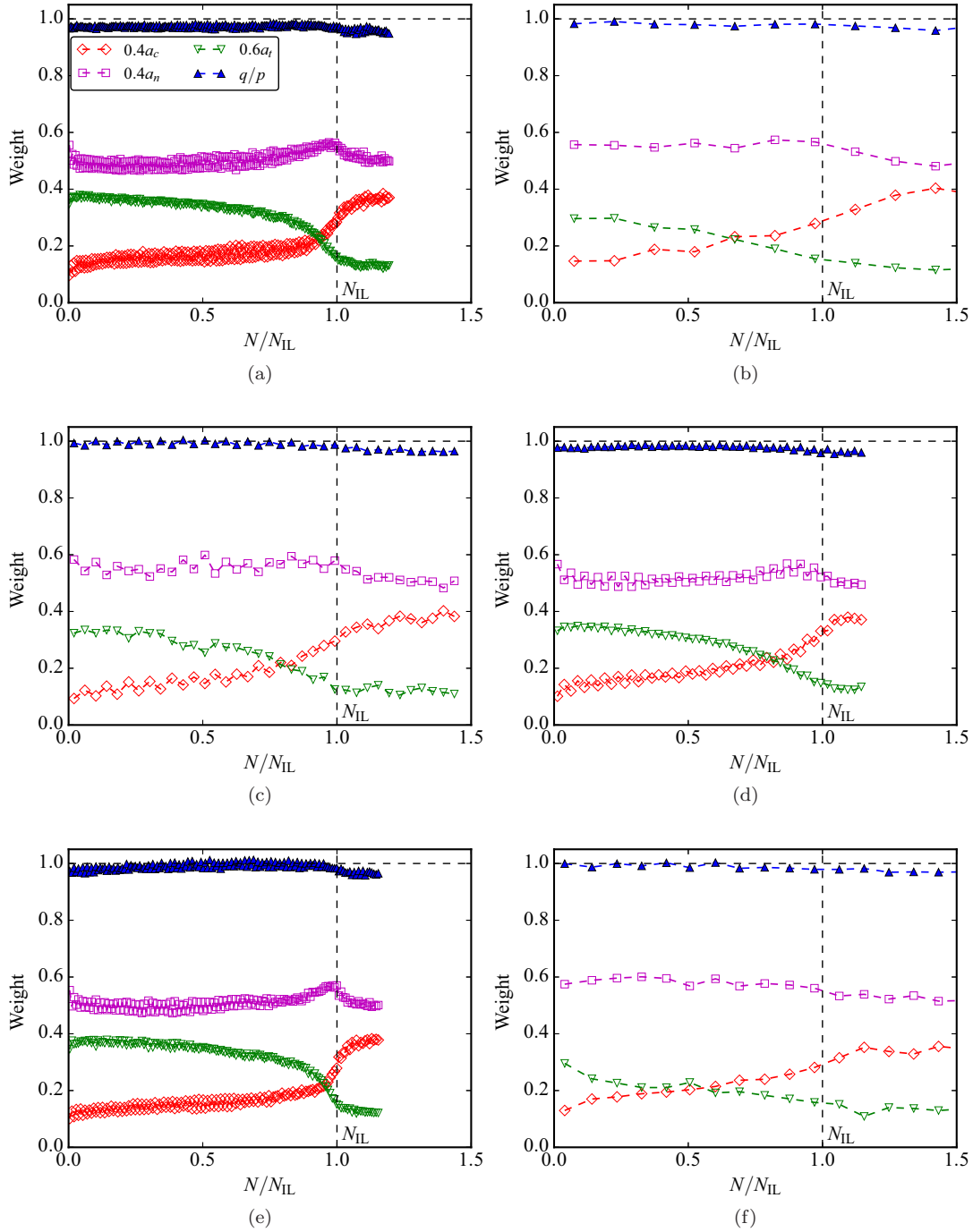


FIG. 17. Evolution of the respective contributions of anisotropies to the stress ratio q/p at $\tau = \pm\tau^{\text{amp}}$ and the theoretical value of q/p according to Eq. (24) for (a) T1, (b) T3, (c) T4, (d) T5, (e) T6, and (f) T7.

simulation. The effects of the initial and loading conditions on these distributions are not significant.

VI. SUMMARY AND DISCUSSION

In this paper, we investigated the highly nonlinear evolution of granular microstructure with isochoric cyclic simple shearing by means of discrete-element numerical simulations and for several different values of the initial mean stress, void ratio, and cyclic stress ratio. The macroscopic behavior is characterized by typical oscillations of shear stress and grad-

ual degradation of the mean stress until the system enters a state of cyclic liquefaction or cyclic mobility. In the transition to the liquefaction state, where the mean stress approaches zero, the coordination number and the nonrattler fraction drop significantly, and the force-bearing network collapses. Unconventional distributions of normal contact forces occur in this state as compared to those in a stable packing.

In the liquefied state, large shear deformation is required to rebuild the contact network and exit the liquefaction state in each cycle, as characterized by the particle connectivity and contact network anisotropy, providing the geometrical

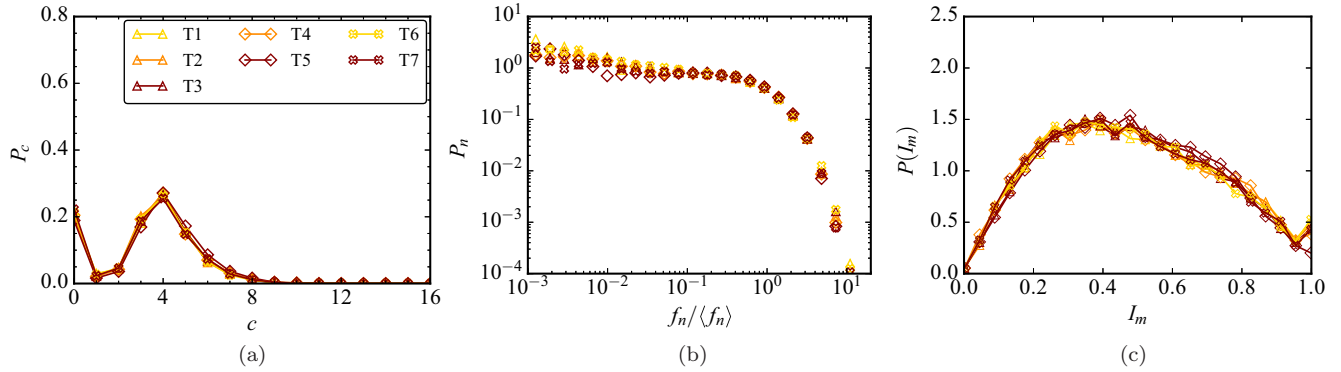


FIG. 18. (a) Particle connectivity diagram, probability density functions of (b) normal forces and (c) mobilized friction index when the shear stress reaches its maximum amplitude in the last simulated cycle.

support for the subsequent shear. The relationship between deviatoric stress ratio and the force and fabric anisotropies was also verified, revealing a nearly constant contribution of the normal force anisotropy, an increasing contribution of the fabric anisotropy, and a decreasing contribution of the tangential force anisotropy or friction mobilization to the deviatoric stress ratio as cyclic shearing proceeds. We also explored the effects of the initial and loading conditions on the microstructural evolution. It was found that in all cases, the transition to the liquefaction state is characterized by a critical value of the coordination number (≈ 3.6) that corresponds to the percolation threshold of the contact network. We also observed a similar evolution of the fabric and force anisotropies, and their saturation values in simulations with different initial and loading conditions.

The hysteresis loops in the postliquefaction period can be viewed as oscillations around an unstable state. Although the coordination number can drop to low values (below the isostatic value), the unjamming occurs at a coordination number of 4, and subsequent jamming leads to a coordination number of 3.6. Before this connectivity is reached, no pressure buildup occurs. In this sense, the coordination number of 3.6 corresponds to the mechanical percolation threshold of the contact network. This value is well above the isostatic coordination number, which is 2 in our simulations. It is also important to remark that the jammed state in each postliquefaction cycle is anisotropic with a fabric anisotropy ≈ 0.75 .

We found that the contact network and mean stress never vanished in our simulations. This is also the case in most reported simulations in the literature, but assumed to be low enough to be neglected. Although the mean stress in the unjammed state is quite low, its nonzero value implies that the phenomenology of cyclic liquefaction does not crucially depend on the condition of strict vanishing of the mean stress. Actually, in asymmetric cyclic loading the mean stress does not vanish, but the mechanical behavior is quite similar to symmetric cyclic shearing [19]. The full vanishing of the mean stress and coordination number may occur for much larger void ratio, but then the void ratio will be too high to allow for re-jamming of the particles at constant volume. Such a limit should exist and merits a parametric investigation. However, what makes cyclic liquefaction important and interesting is the fact that it occurs at low void ratio, and therefore the unjammed state with its vanishing mean stress and coordination

number is different from a dilute suspension in the sense that it is still a dense system that has an anisotropic structure and can easily jam under continued shearing. More generally, this underlines that the stress-bearing capacity of granular materials is crucially dependent on their microstructure rather than the void ratio alone. As most continuum models of granular materials use the void ratio as state variable, they can not account for cyclic shearing unless proper internal variables pertaining to the contact network and characteristic fabric states are introduced. It is by no means obvious that the same internal parameters can be used both before and after the onset of liquefaction.

As we argued that the mechanical states of a granular material under isochoric cyclic shearing are different from those observed under stress-controlled conditions, the force distributions provide a clear example in this respect. While the force PDF is generally quite stable in stress-controlled shearing and only marginally influenced by the development of fabric anisotropy, we found that the force PDF is increasingly more inhomogeneous as the liquefaction state is approached (reflected in the broader exponential fall-off of the number of forces above the mean force). This enhanced inhomogeneity is consistent with the decrease of the coordination number and larger fabric anisotropies reached by the system as cyclic shearing proceeds. The increasing inhomogeneity of contact forces implies an increasingly more pronounced role of force chains. Such chains are propped by weaker forces [67]. However, as cyclic shearing continues and an increasing number of particles with only three contacts appear, the number of weak supporting forces declines and force chains become increasingly more prone to collapse. This is a plausible scenario for transition to the liquefaction state. As force snapshots in Fig. 3 suggest, the initial liquefaction corresponds in this way to the collapse of strong force chains. This collapse occurs without significant loss of anisotropy, meaning that the residual microstructure after unjamming carries a signature of the jammed state with a residual mean stress that can undergo large shear strain before rejamming into a strong network.

This work can be expanded in several directions. Since the liquefaction transition critical coordination number is quite robust with respect to the initial and loading conditions, an issue is how it depends on the sample's inherent properties, such as particle size distribution, particle shape [68], and particle interaction parameters. For example, the effect of

sliding friction coefficient and rolling friction on the liquefaction resistance and transition merit a parametric investigation. The microstructural analysis can also be enriched by a more detailed analysis of the evolution of force correlations and force fluctuations at transition to the liquefaction state [69,70]. The evolution of the pore space [30,71,72] may also be analyzed in this regard. Finally, the dependence of the residual stress, critical coordination number, force PDF, and fabric

evolution can be investigated for a broader range of void ratios.

ACKNOWLEDGMENT

Financial support for this study was provided by the Natural Sciences and Engineering Research Council of Canada (NSERC).

-
- [1] H. M. Jaeger, S. R. Nagel, and R. P. Behringer, Granular solids, liquids, and gases, *Rev. Mod. Phys.* **68**, 1259 (1996).
- [2] F. Radjai, J.-N. Roux, and A. Daouadji, Modeling granular materials: Century-long research across scales, *J. Eng. Mech.* **143**, 04017002 (2017).
- [3] H. B. Seed and I. M. Idriss, Analysis of soil liquefaction: Niigata earthquake, *J. Soil Mech. Found. Div.* **93**, 83 (1967).
- [4] K. Ishihara, Liquefaction and flow failure during earthquakes, *Géotechnique* **43**, 351 (1993).
- [5] J. Kameda, H. Kamiya, H. Masumoto, T. Morisaki, T. Hiratsuka, and C. Inaoi, Fluidized landslides triggered by the liquefaction of subsurface volcanic deposits during the 2018 Iburi-Tobu earthquake, Hokkaido, *Sci. Rep.* **9**, 13119 (2019).
- [6] A. Elgamal, Z. Yang, E. Parra, and A. Ragheb, Modeling of cyclic mobility in saturated cohesionless soils, *Int. J. Plast.* **19**, 883 (2003).
- [7] J.-M. Zhang and G. Wang, Large post-liquefaction deformation of sand, part I: Physical mechanism, constitutive description and numerical algorithm, *Acta Geotechnica* **7**, 69 (2012).
- [8] A. R. Barrero, M. Taiebat, and Y. F. Dafalias, Modeling cyclic shearing of sands in semifluidized regime, *Int. J. Numer. Anal. Methods Geomech.* **44**, 371 (2020).
- [9] M. Yang, M. Taiebat, and Y. F. Dafalias, SANISAND-MSf: A sand plasticity model with memory surface and semifluidised state, *Géotechnique* (2021).
- [10] M. Taiebat, B. Jeremić, Y. F. Dafalias, A. M. Kaynia, and Z. Cheng, Propagation of seismic waves through liquefied soils, *Soil Dyn. Earthquake Eng.* **30**, 236 (2010).
- [11] R. Wang, J.-M. Zhang, and G. Wang, A unified plasticity model for large post-liquefaction shear deformation of sand, *Comput. Geotech.* **59**, 54 (2014).
- [12] J. Ramirez, A. R. Barrero, L. Chen, S. Dashti, A. Ghofrani, M. Taiebat, and P. Arduino, Site response in a layered liquefiable deposit: Evaluation of different numerical tools and methodologies with centrifuge experimental results, *J. Geotech. Geoenviron. Eng.* **144**, 04018073 (2018).
- [13] A. Reyes, M. Yang, A. R. Barrero, and M. Taiebat, Numerical modeling of soil liquefaction using the SANISAND-Sf model in LEAP experiments, *Soil Dyn. Earthquake Eng.* **143**, 106613 (2021).
- [14] A. J. Liu and S. R. Nagel, Jamming is not just cool any more, *Nature (London)* **396**, 21 (1998).
- [15] D. Bi, J. Zhang, B. Chakraborty, and R. P. Behringer, Jamming by shear, *Nature (London)* **480**, 355 (2011).
- [16] M. P. Ciamarra, R. Pastore, M. Nicodemi, and A. Coniglio, Jamming phase diagram for frictional particles, *Phys. Rev. E* **84**, 041308 (2011).
- [17] M. Xu, Z. Zhang, and X. Huang, Identification of jamming transition: A critical appraisal, *Granular Matter* **23**, 5 (2021).
- [18] Y. P. Vaid and S. Sivathayalan, Fundamental factors affecting liquefaction susceptibility of sands, *Can. Geotech. J.* **37**, 592 (2000).
- [19] M. R. Kuhn, H. E. Renken, A. D. Mixsell, and S. L. Kramer, Investigation of cyclic liquefaction with discrete element simulations, *J. Geotech. Geoenviron. Eng.* **140**, 04014075 (2014).
- [20] E. L. Martin, C. Thornton, and S. Utili, Micromechanical investigation of liquefaction of granular media by cyclic 3D DEM tests, *Géotechnique* **70**, 906 (2020).
- [21] F. Radjai and F. Dubois (Eds.), *Discrete-Element Modeling of Granular Materials* (Wiley-Iste, New York, 2011).
- [22] T.-T. Ng and R. Dobry, Numerical simulations of monotonic and cyclic loading of granular soil, *J. Geotech. Eng.* **120**, 388 (1994).
- [23] T. G. Sitharam, J. S. Vinod, and B. V. Ravishankar, Post-liquefaction undrained monotonic behavior of sands: Experiments and DEM simulations, *Géotechnique* **59**, 739 (2009).
- [24] A. Soroush and B. Ferdowsi, Three dimensional discrete element modeling of granular media under cyclic constant volume loading: A micromechanical perspective, *Powder Technol.* **212**, 1 (2011).
- [25] X. Huang, C.-Y. Kwok, K. J. Hanley, and Z. Zhang, DEM analysis of the onset of flow deformation of sands: Linking monotonic and cyclic undrained behaviours, *Acta Geotechnica* **13**, 1061 (2018).
- [26] S. L. Kramer, *Geotechnical Earthquake Engineering* (Prentice Hall, Upper Saddle River, NJ, 1996).
- [27] T. G. Sitharam, Discrete element modeling of cyclic behavior of granular materials, *Geotech. Geol. Eng.* **21**, 297 (2003).
- [28] T. M. Evans and L. Zhang, A numerical study of particle friction and initial state effects on the liquefaction of granular assemblies, *Soil Dyn. Earthquake Eng.* **126**, 105773 (2019).
- [29] F. Radjai and V. Richefeu, Bond anisotropy and cohesion of wet granular materials, *Philos. Trans. R. Soc., A* **367**, 5123 (2009).
- [30] G. Wang and J. Wei, Microstructure evolution of granular soils in cyclic mobility and post-liquefaction process, *Granular Matter* **18**, 51 (2016).
- [31] R. Wang, P. Fu, J.-M. Zhang, and Y. F. Dafalias, DEM study of fabric features governing undrained post-liquefaction shear deformation of sand, *Acta Geotechnica* **11**, 1321 (2016).
- [32] P. Mutabaruka, Numerical modeling of immersed granular media: initiation and propagation of avalanches in a fluid, Ph.D. thesis, Université Montpellier II—Science and Technology of Languedoc, Montpellier, France, 2013.
- [33] S. Luding, Cohesive, frictional powders: Contact models for tension, *Granular Matter* **10**, 235 (2008).

- [34] C. Voivret, F. Radjaï, J.-Y. Delenne, and M. S. El Youssoufi, Space-filling properties of polydisperse granular media, *Phys. Rev. E* **76**, 021301 (2007).
- [35] P. Mutabaruka, M. Taiebat, Roland J.-M. Pellenq, and F. Radjai, Effects of size polydispersity on random close-packed configurations of spherical particles, *Phys. Rev. E* **100**, 042906 (2019).
- [36] C. Thornton, *Granular Dynamics, Contact Mechanics and Particle System Simulations* (Springer, 2015).
- [37] C. Thornton, Numerical simulations of deviatoric shear deformation of granular media, *Géotechnique* **50**, 43 (2000).
- [38] C. O'Sullivan, *Particulate Discrete Element Modeling: A Geomechanics Perspective* (CRC Press, Boca Raton, FL, 2011).
- [39] G. D. R. MiDi, On dense granular flows, *Eur. Phys. J. E* **14**, 341 (2004).
- [40] T. Schwager and T. Pöschel, Coefficient of restitution and linear-dashpot model revisited, *Granular Matter* **9**, 465 (2007).
- [41] N. Guo and J. Zhao, The signature of shear-induced anisotropy in granular media, *Comput. Geotech.* **47**, 1 (2013).
- [42] M. Jiang, A. Zhang, and T. Li, Distinct element analysis of the microstructure evolution in granular soils under cyclic loading, *Granular Matter* **21**, 39 (2019).
- [43] R. Dyvik, S. Lacasse, T. Berre, and B. Raadim, Comparison of truly undrained and constant volume direct simple shear tests, *Géotechnique* **37**, 3 (1987).
- [44] S. Yimsiri and K. Soga, DEM analysis of soil fabric effects on behavior of sand, *Géotechnique* **60**, 483 (2010).
- [45] Z.-X. Wu, C. Dano, P.-Y. Hicher, and Z.-Y. Yin, Estimating normal effective stress degradation in sand under undrained simple shear condition, *Eur. J. Environ. Civil Eng.* **25**, 170 (2021).
- [46] X. Huang, K. J. Hanley, Z. Zhang, C.-Y. Kwok, and M. Xu, Jamming analysis on the behaviours of liquefied sand and virgin sand subject to monotonic undrained shearing, *Comput. Geotech.* **111**, 112 (2019).
- [47] F. Radjai, H. Troadec, and S. Roux, Key features of granular plasticity, in *Granular Materials: Fundamentals and Applications*, edited by S. Antony, W. Hoyle, and Y. Ding (Cambridge University Press, Cambridge, 2004), pp. 157–184.
- [48] K. Shundyak, M. van Hecke, and W. van Saarloos, Force mobilization and generalized isotaticity in jammed packings of frictional grains, *Phys. Rev. E* **75**, 010301(R) (2007).
- [49] X. Huang, K. J. Hanley, Z. Zhang, and C.-y. Kwok, Structural degradation of sands during cyclic liquefaction: Insight from DEM simulations, *Comput. Geotech.* **114**, 103139 (2019).
- [50] F. Radjai, M. Jean, J.-J. Moreau, and S. Roux, Force Distribution in Dense Two-Dimensional Granular Systems, *Phys. Rev. Lett.* **77**, 274 (1996).
- [51] T. S. Majmudar and R. P. Behringer, Contact force measurements and stress-induced anisotropy in granular materials, *Nature (London)* **435**, 1079 (2005).
- [52] F. Radjai, Modeling force transmission in granular materials, *C. R. Phys.* **16**, 3 (2015).
- [53] E. Azema, F. Radjai, R. Peyroux, and G. Saussine, Force transmission in a packing of pentagonal particles, *Phys. Rev. E* **76**, 011301 (2007).
- [54] V. Richefeu, M. S. El Youssoufi, E. Azéma, and F. Radjai, Force transmission in dry and wet granular media, *Powder Technol.* **190**, 258 (2009).
- [55] D. Cantor, E. Azéma, P. Sornay, and F. Radjai, Rheology and structure of polydisperse three-dimensional packings of spheres, *Phys. Rev. E* **98**, 052910 (2018).
- [56] F. Radjaï, S. Roux, and J. J. Moreau, Contact forces in a granular packing, *Chaos* **9**, 544 (1999).
- [57] E. Azema and F. Radjai, Force chains and contact network topology in sheared packings of elongated particles, *Phys. Rev. E* **85**, 031303 (2012).
- [58] K.-I. Kanatani, Distribution of directional data and fabric tensors, *Int. J. Eng. Sci.* **22**, 149 (1984).
- [59] E. Azema, F. Radjai, and F. Dubois, Packings of irregular polyhedral particles: Strength, structure, and effects of angularity, *Phys. Rev. E* **87**, 062203 (2013).
- [60] M. Oda, Fabric tensor for discontinuous geological materials, *Soils Foundations* **22**, 96 (1982).
- [61] M. Satake, Fabric tensor in granular materials, in *Deformation and Failure of Granular Materials*, edited by P. A. Vermeer and H. J. Lager (CRC Press, Balkema, Rotterdam, 1982), pp. 63–68.
- [62] H. Ouadfel and L. Rothenburg, “Stress–force–fabric” relationship for assemblies of ellipsoids, *Mech. Mater.* **33**, 201 (2001).
- [63] L. Rothenburg and R. J. Bathurst, Analytical study of induced anisotropy in idealized granular materials, *Géotechnique* **39**, 601 (1989).
- [64] E. Azéma and F. Radjaï, Internal Structure of Inertial Granular Flows, *Phys. Rev. Lett.* **112**, 078001 (2014).
- [65] F. Radjai, J.-Y. Delenne, É. Azema, and S. Roux, Fabric evolution and accessible geometrical states in granular materials, *Granular Matter* **14**, 259 (2012).
- [66] I. Agnolin and J.-N. Roux, Internal states of model isotropic granular packings. II. Compression and pressure cycles, *Phys. Rev. E* **76**, 061303 (2007).
- [67] F. Radjai, D. E. Wolf, M. Jean, and J. J. Moreau, Bimodal Character of Stress Transmission in Granular Packings, *Phys. Rev. Lett.* **80**, 61 (1998).
- [68] D.-H. Nguyen, E. Azéma, P. Sornay, and F. Radjaï, Effects of shape and size polydispersity on strength properties of granular materials, *Phys. Rev. E* **91**, 032203 (2015).
- [69] J. F. Peters, M. Muthuswamy, J. Wibowo, and A. Tordesillas, Characterization of force chains in granular material, *Phys. Rev. E* **72**, 041307 (2005).
- [70] S. Amirrahmat, W. H. Imseeh, K. A. Alshibli, P. Kenesei, Z. A. Jarrar, and H. Sharma, 3D experimental measurements of evolution of force chains in natural silica sand, *J. Geotech. Geoenviron. Eng.* **146**, 04020027 (2020).
- [71] A. Sufian, A. R. Russell, A. J. Whittle, and M. Saadatfar, Pore shapes, volume distribution and orientations in monodisperse granular assemblies, *Granular Matter* **17**, 727 (2015).
- [72] A. Sufian, A. R. Russell, and A. J. Whittle, Evolving pore orientation, shape and size in sheared granular assemblies, *Granular Matter* **21**, 4 (2019).